Generation of Engineered Aerosol Stainless Steel Nanoparticles using a Spark Discharge Generator

Author

Calle Preger

Supervisors

Maria Messing

Linus Ludvigsson

Per-Olof Larsson

Examiner

Carina Fasth

2016-02-03

Populärvetenskaplig Sammanfattning

För första gången har luftburna nanopartiklar av rostfritt stål skapats med en gnistgenerator. Dessa nanopartiklar kan användas till att skapa strukturer som tidigare inte varit möjliga samt att förbättra processen när man tillverkar metalldelar från ett metallpulver så att detta kan ske vid lägre temperatur och på så vis spara energi.

Framsteg

För första gången har luftburna nanopartiklar av rostfritt stål skapats med en specifik storlek i storleksintervallet 30-50 nm. Nanopartiklarna fick liknande innehåll som de stålstavar som användes vid genereringen vilket möjliggör generering av nanopartiklar av alla typer av rostfritt stål.

Skapandet av Nanopartiklarna

Metoden som använts för att skapa dessa nanopartiklarna har varit med en gnistgenerator. Två stavar i metall är separerade av ett kort avstånd, stavarna laddas upp och en kort gnista skapas mellan stavarna. Gnistan gör att material från stavens yta förångas och det förångade materialet kolliderar och bildar nanopartiklar. Nanopartiklarna kommer ha samma innehåll som stavarna vilket möjliggör kombinationer av de allra flesta metaller. Att nanopartiklarna är luftburna ger mycket större kontroll över processen jämfört med om de skulle skapats i en kemisk lösning. Det är möjligt att välja ut en specifik storlek på partiklarna med mycket hög upplösning förutsatt att partiklarna är formade som klot. Dessutom är det enkelt att mäta partiklarna och förändras deras egenskaper utan att de behöver lyftas ut ur systemet, vilket förenklar själva genereringen. Detta kan vara av stor betydelse om det är viktigt för tillämpningen att alla partiklarna är identiska. Med gnistgeneratorn kan man skapa nanopartiklar på ett billigt och energieffektivt sätt. Dessutom undviker man kemiskt avfall som ofta är en biprodukt när man skapar nanopartiklar.

Nanopartiklar av Rostfritt Stål

En nanopartikel är en partikel med en diameter mellan 1 och 100 nm. Fördelen med nanopartiklar jämfört med större mikro- och makropartiklar är deras stora yta i förhållande till volym. Detta gör att partiklarna är mycket reaktiva och används ofta vid katalytiska processer. Rostfritt stål är en kombination av järn och krom. Eftersom järn lätt oxiderar och rostar blandas det med 10-20% krom. Kromet bildar ett skyddande ytskikt som omöjliggör för syret att nå ner till järnet och materialet blir på så vis rostfritt. Det är viktigt att varje nanopartikel av rostfritt stål innehåller tillräckligt mycket krom för att skapa det skyddande ytskiktet och på så vis vara stabila i luft. Vi har inte kunnat visa att detta ytskikt existerar men preliminära resultat indikerar att så är fallet.

Framtidsutsikter

Nanopartiklar av rostfritt stål kan komma att användas i flera olika områden. Det är dock viktigt att de används på ett korrekt sätt så att de inte blir hälsofarliga för omgivningen. Dessa nanopartiklar skulle kunna användas när man pressar ihop ett metallpulver under upphettning till en färdig fast struktur. Nanopartiklarna kan möjliggöra att detta kan ske vid lägre upphettningstemperaturer och på så vis spara energi, dessutom kan de mekaniska egenskaperna på den färdiga strukturen förbättras. Nanopartiklarna kommer under denna process konsumeras och det finns ingen risk för den som använder den slutgiltiga produkten att exponeras för nanopartiklarna. Dessa små nanopartiklar skulle också kunna användas som byggstenar för att skapa detaljrika mikrometerstora strukturer i rostfritt stål vid 3D-printning.

Abstract

This diploma work has shown that it is possible to generate engineered stainless steel nanoparticles using a spark discharge generator (SDG) with a selectable size in the size range 20-70 nm in diameter. The generated particles have similar composition as the electrodes used, although further studies are needed to verify if this is true for all particles generated. If this is true, it would be possible to produce nanoparticles of any type of stainless steel alloy - the only prerequisite is that it exists in bulk form. The most suitable operating parameters for the generation have been determined to: 2 mm gap distance between the electrodes and 10 mA charging current when the capacitance was 21 nF. The compaction temperature was determined to be approximately $1200°C$ when 50 nm agglomerates were compacted in nitrogen. It is still uncertain whether it exists a protective chromium oxide layer surrounding each particle and making it corrosion resistant. The chromium content in the particles indicates that there might be and the particles are stable in air but more research is needed to conclude this. A complete study on engineered stainless steel nanoparticles has not been performed and more research needs to be done, different types of carrier gas need to be tested to optimize for higher concentration, lower compaction temperature and avoiding possible nitride formation and oxidation. Also, more TEM and XEDS studies need to be performed in order to determine the average composition of the nanoparticles. An experiment when these nanoparticles were used to enhance sintering behavior of a micro-powder was initiated but not completed and needs to be investigated further. The results in this work can be used as a base for further studies on engineered stainless steel nanoparticles.

Nomenclature

AISI   **A**merican **I**ron and **S**teel **I**nstitute

bcc   **b**ody-**c**entered **c**ubic

BSE   **B**ack **S**cattered **E**lectrons

DMA   **D**ifferential **M**obility **A**nalyzer

ENP   **E**ngineered **N**ano**P**articles

SDG   **S**park **D**ischarge **G**enerator

SEM   **S**canning **E**lectron **M**icroscope

SE   **S**econdary **E**lectrons

STEM   **S**canning **T**ransmission **E**lectron **M**icroscopy

TEM   **T**ransmission **E**lectron **M**icroscope

XEDS   **E**nergy **D**ispersive **X**-ray **S**pectroscopy

Z   Atomic number

Contents

1 Introduction

The constant need for our society to develop and grow has increased the need of nanostructures. To "do more with less" is one of the main reasons why nanotechnology is of great interest around the world. Also, at the nanometer scale, materials does not act in the same way as in makro scale and new properties and features appears, quantum mechanical effects are more important as well as surface reactivity. A nanostructure needs to have, at least, one dimension sized from 1-100 nm and one type of nanostructure is a nanoparticle. It is defined as a particle with a diameter between 1 and 100 nm. Naturally occurring nanoparticles are very common and could be generated as an unwanted product during combustion, road wear or when burning candles [1]. However, Engineered nanoparticles (ENP) are particles generated in a controlled environment with tailored properties such as size and composition. The main feature of ENP compared to larger microparticles is the large surface to volume ratio. The smaller the particle, the larger this ratio becomes. Since most chemical and physical reactions happen on the surface, ENP are very reactive and are frequently used as catalysts [2].

An aerosol is a particle that is suspended in a gas and ENP produced in the aerosol phase are of great interest since it enables good control of particle size, morphology and purity [3]. These aerosol ENP have already been used in many applications including growth of nanowires that are used in photovoltaics cells and light-emitting diodes [4]. Some of the techniques used to generate ENP are laser ablation, flame spray pyrolysis and furnace reactions. All these have different limiting factors; flame spray pyrolysis is used to produce bulk quantities of metal oxides but is limited in production of pure metals and different precursors are needed. Furnace reactions are very energy consuming since the furnace needs to be heated to high temperature and laser ablation is a very expensive technique [3, 5].

A promising technique that avoids all these limiting factors is the evaporation/condensation technique by using a Spark Discharge Generator (SDG). It is cheap, does not produce any chemical waste and enables production of pure aerosol nanoparticles with a narrow size distribution in the entire nanometer range (1-100 nm) [6]. Another great advantage with the SDG method is the large variety of materials that can be produced. The SDG has been successfully used to form nanoparticles containing highly pure single element particles [7], alloyed particles [8] and has even been used to form particles of materials that are immiscible in bulk [9].

In a SDG aerosol nanoparticles are formed due to the creation of a plasma channel that leads to a discharge, a spark, between two conducting electrodes. This spark evaporates material from the electrodes and the evaporated material collide and becomes particles. [10]. This technique is well established and firmly described in detail in many reports [8, 10, 11]. However, although the technique was established already in 1988 the details regarding particles formation are still not fully understood and further studies are needed [12, 13]. During four years, the European Union initiative BUONAPART-E has been focusing on large up-scale of nanoparticles generated by this technique and substantial progress has been made.

Stainless steel is a complex alloy that exists in many different composition with different properties. It has good corrosion resistance, strength and useful magnetic properties, which makes it important for many industrial companies. The complexity of stainless steel arises because it consists of many different phases and the phase of the material depends on how it is processed [14]. An interesting aspect with stainless steel nanoparticles generation is what type of phase the particles will form and how the mixing will be. If the particles are homogeneously mixed or if it forms islands inside the particles with an alternative compositions.

The first aim with this thesis was to investigate whether it is possible to generate stainless steel nanoparticles using a SDG. Also to characterize these particles based on size, shape, concentration and properties. If all this is possible, also start investigate different applications using these nanoparticles. To do so two different type of stainless steel electrodes were used, AISI 410 and AISI 430.

Höganäs AB specializes in metallic powders and is the worlds largest producer of iron powder [15]. They fabricate powder with an average diameter in the micrometer range that are later used to form larger solid structures. Two of the reasons to use micro-powders to form metallic

gears instead of bulk material are the lowered cost and the high material utilization with little waste. Therefore, using micro-powder is a fast, environmentally friendly and non-expensive way to produce metallic gears. The size of the particles in the powder is of large importance in the sintering process. Smaller particles have higher surface energy and the main driving force in the sintering process is the elimination of surface energy of the particles in the powder. Therefore, will smaller particles sinter faster and at lower temperatures compare to larger particles [16].

Stainless steel nanoparticles have with its small size and high surface energy the possibility to improve the properties of metallic powders. The only drawback with the nanoparticle generation is the low output. Höganäs AB produces tons of powders each day and trying to generate a powder completely out of nanoparticles is not possible. However, these nanoparticles could possibly be used to enhance the sintering properties and enable sintering at lower temperatures when being deposited onto a micro-powder. This could also increase the final density and improve the mechanical properties of the resulting solid structure [17].

The second aim with this thesis was to investigate whether it is possible to enhance sintering of a micro-powder by depositing aerosol stainless steel nanoparticles onto a micro-powder.

2 Theory

2.1 Stainless Steel

The steel industry employs about 50 000 persons in Sweden today and its export contributes greatly to GNP and tax revenues [18]. Steel is a combination of iron and a small amount of carbon. The carbon atoms are located at interstitial sites between the iron atoms and the addition of carbon will both increase the strength and weldability of the steel. Steel can easily be melted and reused again and this fact together with the common elements makes steel a very inexpensive material. One drawback is that steel, similar to iron, easily corrodes. Stainless steel, however, is known for having good corrosion resistance and is therefore a much better option in many applications. To transform steel into stainless steel the structure needs to have at least 11 wt.% chromium [19]. The chromium and iron are occupying the same lattice sites but the chromium will oxidize much faster than the iron and when it does it forms a thin, stable oxide film at the surface, approximately 2 nm thick. This layer protects the underlying steel from oxidizing and degrading and the steel is then said to be passivated [14]. The corrosion resistance increases with increased chromium content and the type of stainless steel with highest resistance normally have a chromium content >18 wt.% [19]. The main drawback with chromium is that it tends to be more reactive than iron and easily form carbides, nitrides and sulfides [14].

Stainless steel is an alloy that exists in many different compositions and elements, each alloy with its own special property. It always contains iron and chromium but could also contain nickel or manganese to make it less magnetic or brittle at lower temperatures. Most stainless steel alloys contain a small fraction of silicon, phosphorous, sulfur and nitrogen, however, these elements will not have a major effect on the final properties [14].

2.1.1 Ferritic Stainless Steel

Ferritic stainless steel is a class of stainless steel with a high chromium content, always higher than 12 wt% [14]. The melting point is slightly lower than pure iron and in room temperature are all ferritic stainless steels in the phase ferrite. This phase has a body-centered cubic (bcc) structure and is normally denoted with an α, see Figure 1. The carbon content in a ferritic stainless steel is normally low, $\sim$0.1 wt.% [14]. Chromium is a strong carbide-forming element and a higher carbon content will also result in unwanted chromium carbides. The chemical formulas for the most common carbides that forms in these structures are $K_1(=M_{23}C_6)$ and $K_2(=M_7C_3)$, where M is iron or chromium. The first carbide mentioned, K_1 is often formed along the grain boundaries where it will promote local corrosion, so called intergranular corrosion, and lower the quality of the steel. Also, the formation of chromium carbides could deplete the surrounding matrix to contain less than 12 wt.% chromium, making it susceptible to corrosion. The steel is then said to be sensitized and loses its ability to resist corrosion. Because of this, most stainless steels have a low and sometimes negligible carbon content [14].

A commonly used type of ferritic stainless steel is the AISI 430. The content is usually max 0.12 wt.%C and 16-18 wt.%Cr, also manganese and silicon are usually present each with maximum 1 wt.% [14].
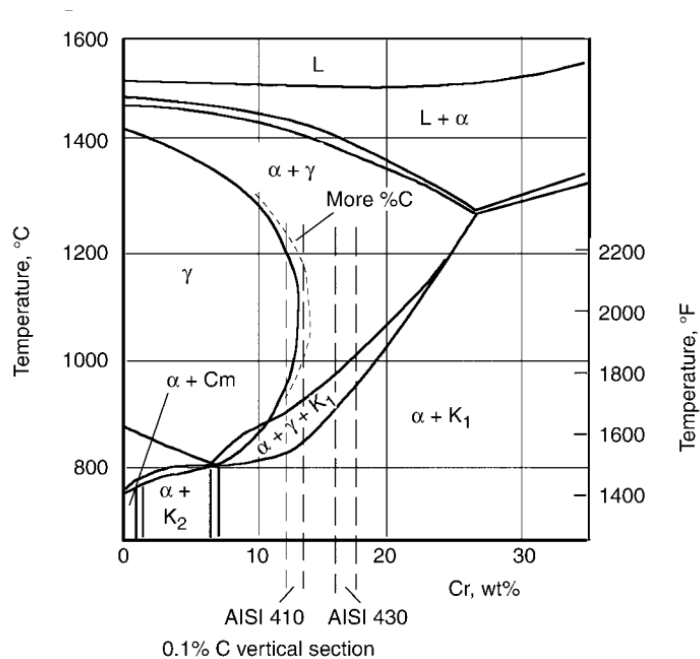
Figure 1: Ternary phase diagram of Cr-Fe-C, with chromium content on x-axis and an increased carbon content in between vertical lines [20].
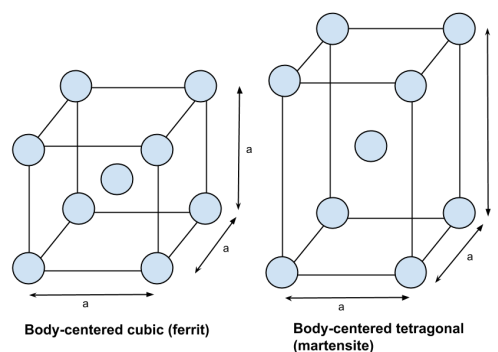

Figure 2: The two different crystal structures of ferrit and martensite.

2.1.2 Martensitic Stainless Steel

The martensitic stainless steel has a lower chromium content compared to the ferritic stainless steel. In similarity with the ferritic stainless steel, martensitic also form K_1 carbides upon cooling. This formation will be inhibited if the sample is cooled very quickly and the corrosion resistance will be stronger. However, the corrosion resistance is normally much weaker for martensitic compared to the ferritic stainless steel due to lower chromium content. The bcc crystal structure will be distorted if the carbon content is increased in the martensitic structure. One of the lattice sides will increases in length and a new crystal structure, called body-centered tetragonal (bct), will be formed, see Figure 2 [14].

The AISI 410 is one of the most commonly used martensitic stainless steel. In the temperature range 1000 to 1200°C, the AISI 410 only contains the phase austenite, denoted with a γ, but both above and below this temperature region it contains ferrite, see Figure 1 [14, 20]. Both ferritic and

4

martensitic stainless steel are classed as ferromagnetic with a high permeability and low coercive force, making both types a soft magnet and becomes magnetic in the presence of a magnetic field. The permeability for ferritic is larger than the martensitic [21].

2.2 Sintering of Powders

The main reason to use metal powders to form metal structures instead of bulk processes is the lower costs. It is possible to form near net shape components with a high material utilization and with little scrap. Using a low-cost powder to form complex parts for industry have economical reasons. Instead of using several complex steps, can gears out of powders be formed with a few simple steps. Some material and material properties are hard to generate without using a powder such as high-temperature materials and porous filters [16].

Sintering is the process when compacting and forming a solid mass out of material by heat and/or pressure without melting it to the point of liquefaction. It is usually performed by pressing and heating a powder into a solid structure. The driving force of the sintering process is the elimination of surface energy. Smaller particles will have higher surface energy and the driving force to sinter will be larger [16]. The end product will also reach a higher final density if the particles in the powders are smaller. The density could reach almost 100% with no pores present in final structure if the initial size of the particles in the powder is small enough [17]. This driving force to sinter can be describe as the stress, σ, associated with curved surfaces,

$$\sigma = \frac{\gamma}{\frac{1}{R_1} + \frac{1}{R_2}} \tag{1}$$

where γ is the surface energy and R_1 and R_2 are the radii of two adjacent particles. A completely flat surface will according to this equation be a stress free surface and has no driving force to sinter [16]. At the beginning of the sintering process, a region between the two particles arises called the neck region. Atoms from the two particles are moving into this region and it increases in size as the sintering process proceeds, see Figure 3. If Equation 1 was described with respect to neck size and diameter of the particles instead of radius, the driving force would be described as following,

$$\sigma = \gamma\left(\frac{2}{X} - \frac{4D}{X^2}\right) \tag{2}$$

where D is the diameter of the particle and X is the neck size. Because of the square dependence of X, the stress will be high when the neck size is small. When two particles collide, the neck size will be small, almost zero, and the stress will be very high. This results in a quick sintering process and the neck region will grow rapidly. With time, this neck size becomes equal to the initial diameter of the particles and the shape between the two particles will be flat. The driving force then becomes zero [16].
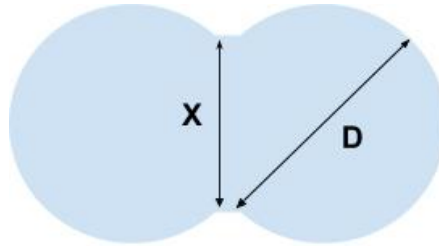

Figure 3: Necking of two adjacent particles. D is the diameter of the spherical particle and X is the neck size.

If introducing a large amount of nanoparticles to the surface of the particles in the micro-powder it will create a large amount of small regions with very small neck size compared to the diameter. This will generate a high driving force to sinter at very many positions at the same time and will enhance the sintering process of the powder. A recent study has shown that when mixing a micro-powder with nanoparticles and forming the structure with powder injection molding both the densification is improved and the sintering could occur at lower temperatures. In this study a relative density of 85% was reached at 1200°C for the nominal micro-powder but was reached at only 1100°C when using a mixture of micro-powder and nanoparticles [17]. The nanoparticles will be consumed during sintering and are therefore of no risk for the end consumer of the product. Making this a harmless application of metallic nanoparticles.

2.3 Spark Discharge Generator (SDG)

2.3.1 The Setup of the Aerosol Nanoparticle Generation

The SDG used in this project has a simple setup consisting of two opposing electrodes located inside a housing chamber with a carrier gas entering from the top of the chamber and exiting at the bottom. This gas is connected to the entire system. The electric setup of this chamber is described more in detail in Section 2.3.2. To characterize and further process the generated particles, the SDG is a part of an aerosol nanoparticle generation setup. This setup includes; one neutralizer, two Differential Mobility Analyzers (DMA), one furnace, one electrometer and one deposition chamber where an electroplate is located. The different parts are connected through simple valves making it easy to add or bypass features in the setup, see Figure 4.

The carrier gas is flowing through the first chamber and is then, after passing through the neutralizer, directed towards the DMAs and the furnace. The DMAs are used to size select the particles but also, in combination with an electrometer, used to measure the size distributions. The furnace is used to compact the particles to make them more spherical and the electrometer is the last tool of the setup and is where the number of particles is measured. It is also possible to deposit particles onto an electroplate located in the deposition chamber, a so called electrostatic precipitator, to make it possible to evaluate the particles outside the system in, for instance, an electron microscope [22].
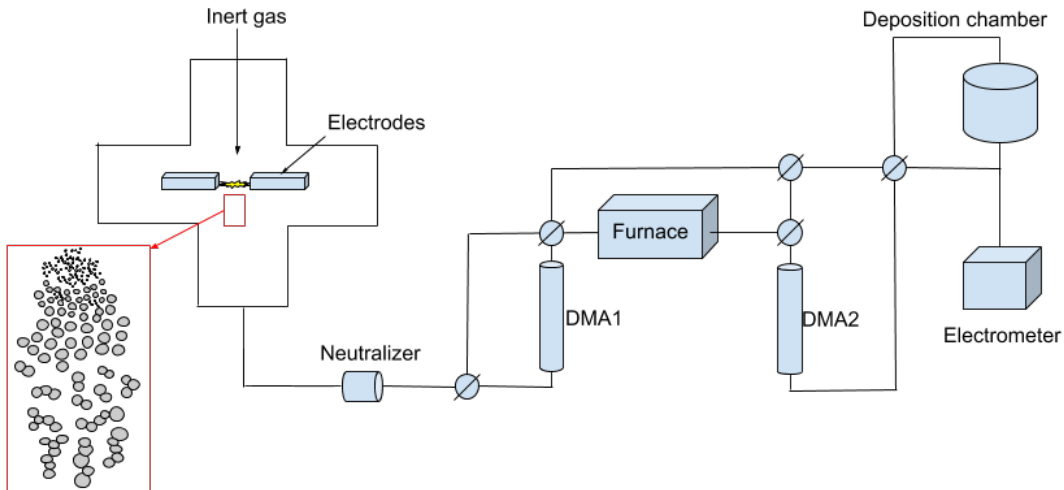

Figure 4: Schematic of the aerosol nanoparticle generation setup including the SDG.

2.3.2 Electronic Setup of the SDG

The electronic setup for the spark generation is a simple RCL circuit, see Figure 5, and is based on the one proposed by Schwyn *et al.* 1988 [23]. A variable capacitor, placed in parallel with the electrodes, is charged by a high voltage power supply and when provided enough energy, a spark is generated in the gap between the electrodes. The gap between the electrodes acts as a resistance and the inductance arises from the cables in the system [11].
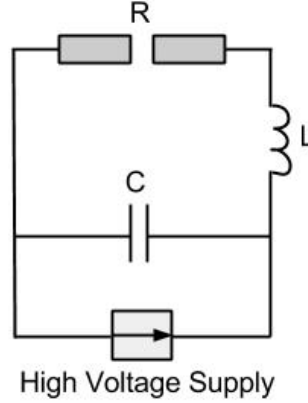

Figure 5: Schematic of the electronic setup of the SDG, the gap between the electrodes acts as resistance.

2.3.3 The Spark

When the capacitor is charged, a high electric field is generated between the two electrodes. In this field, electrons and ions from the carrier gas are accelerated and will eventually gain sufficient amount of energy to ionize further gas molecules. When the energy of the electric field increases, these ionized gas molecules will start ionize several gas molecules and this will induce an avalanche of charged molecules. The gas breaks down and a conductive plasma channel is generated in the gap between the electrodes, this channel thermally expands before a shock wave, the spark, is generated. This results in a brief current between the electrodes that last for a few μs [10]. The rapid discharge is associated with a very high local temperature (20000 K) making the electrode material evaporate. The evaporated material will supersaturate the volume between the electrodes and will nucleate into primary particles as the surrounding gas is rapidly cooled due to an adiabatic expansion [10, 11]. These primary particles are normally in the size range of 1-9 nm [10].

The amount of material evaporated and the concentration and size of the primary particles will later determine the final concentration and size of the nanoparticles generated. This can be controlled by varying the energy of the spark as well as the spark frequency. The energy of the spark, E, is given by the following equation,

$$E = \frac{1}{2}CV_d^2 \tag{3}$$

where C is the capacitance and V_d is the discharge voltage. The capacitance is normally fixed for each experiment but could easily be altered between experiments. The discharge voltage is easy to measure and regulate but more difficult to predict. It is given by the sum of the breakdown voltage, V_b, and an over voltage, V_0.

$$V_d = V_b + V_0 \tag{4}$$

The breakdown voltage is the amount of voltage needed for the gas to break down and for the plasma channel, and spark, to be generated. However, the reason why measuring the discharge voltage instead of the breakdown voltage is because the charging of the capacitor normally occurs
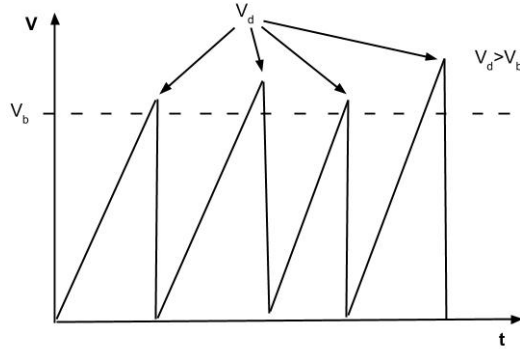
Figure 6: The voltage appearance between the gap vs time, the breakdown voltage, V_b, is always smaller than the discharge voltage, V_d.

very rapidly and this results in an overshoot, see Figure 6. If the charging would have been infinitely slow, the discharge voltage would be equal to the breakdown voltage [11]. However, this is almost never the case, instead the discharge voltage is always larger and that is why it is measured. The breakdown voltage can be determined for each new system since it is governed by Paschen's Law [10]:

$$V_b = \frac{Bpd}{\ln \frac{Apd}{\ln(1+1/\gamma)}} \qquad (5)$$

where A, B and γ are material depending properties of the carrier gas, p is the pressure in the chamber and d is the gap distance between the electrodes. The breakdown voltage will increase with higher gap distance and pressure, however, the exact value depends on the properties of the carrier gas. For instance, air has a significantly higher breakdown voltage than argon and helium. Also, the breakdown voltage for air increases much faster with increased gap distance and pressure compared to argon and helium. A higher breakdown voltage will increase the energy of the spark, see Equation 3, and so will the amount of material evaporated [10]. Another way to increase the particle output is to increase the frequency of the spark, *f*. It is adjusted through the charging current, *I*, and is given by

$$f = \frac{I}{CV_d} \qquad (6)$$

a higher charging current result in a higher spark frequency. If the carrier gas flow is high enough to clear the gap from particles between each spark, a higher frequency will generate more particles per minute [23].

2.3.4 Electrodes

The choice of the material of the electrode as well as the distance between the electrodes are crucial for the particle generation. The electrodes are the only source of material and it determines the elemental composition of the resulting particles. Different compositions of the electrodes have been used to generate particles with a large variety of compositions; identical electrodes have been used to create stable mono metallic nanoparticles [7], two electrodes consisting of different material have been used to generate alloyed nanoparticles [24]. Alloyed electrodes have been used to generate alloyed nanoparticles [6] and also compacted electrodes have been used to generate nanoparticles of material that are immiscible in bulk [9]. The only requirements are that the electrodes should be conducting or semiconducting and also thermally stable [11].

The energy of the spark depends on the distance between the two electrodes. The distance is normally in the mm-range and larger distances will generate sparks with a higher energy, see Equation 5. The location of the sparks could also affect the particle outcome. If the electrode end surface is flat, the locations of the spots where the sparks hits will change each time. If it instead
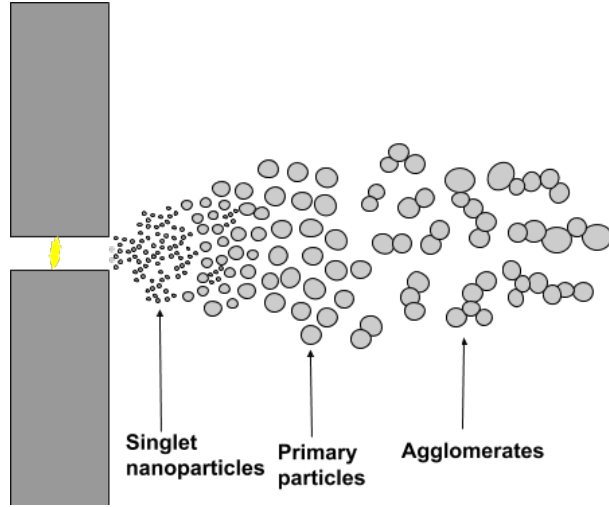
Figure 7: Schematic of the formation of primary particles and agglomerates in the vicinity of the spark.

is sharp, the sparks will hit similar spots each time, however, a sharp electrode will wear out much faster compared to a flat surface and this will change the gap distance much faster. [10, 11].

2.3.5 Particle Formation

Upon formation of primary particles the vapor consists of so called singlet nanoparticles that will grow by complete coalescence or condensation when colliding. This will continues until the singlet nanoparticles reaches a critical size and become primary particles. These primary particles continues to collide and grow but instead of growing with complete coalescence, they will grow by sticking and forming agglomerates, see Figure 7. The singlet nanoparticles are in the size range from a few atoms to a few nanometers in diameter [12]. When they collide and coalesce, the surface energy of these particles decreases and energy is released which will heat the particles. The resulting size of a primary particle will both depend on the time before next collision, τ_c, and the time it takes for the particle to be cooled down by the surrounding gas after coalescence, τ_{cool} [25]. A high concentration of polydisperse singlet particles will result in a low τ_c. When $\tau_c < \tau_{cool}$ the singlet nanoparticle will grow by complete coalescence, but when $\tau_c > \tau_{cool}$ the complete coalescence cease to act and it marks the end of singlet growth and the primary particle is formed. This primary particle will continue to collide but instead of becoming a larger spherical particle, these collisions will result in formation of a non-spherical agglomerate [11, 25]. These agglomerates typically contain several primary particles held together by strong bonds and when agglomerates collides they forms larger agglomerates held together by weak bonds. The morphology of these agglomerates depends on random collision, however, the size can be tuned by varying the concentration of primary particles [3].

There is a large size difference between the diameters of the singlet nanoparticles and the resulting primary particles. The size of singlet nanoparticles and the environment at which they collide and grow will later determine the size of the resulting primary particles as well as the concentration of nanoparticles. The size of the primary particles is hard, but possible, to tune by changing operating parameters. A higher carrier gas flow will, for instance, generate smaller primary particles and by carefully varying the flow rate and the mass production rate, tailored primary particles can be formed [12, 13].

The evaporated material is cooled quickly by the surrounding gas. This fast cooling is crucial for the composition of the agglomerates. If the cooling were to happen at a much slower rate, the vapor would have first formed a stable nuclei on which vapor could condense and particles grow. But when the vapor is quenched, the supersaturation is extremely high and the critical nucleus size can be pushed down to atomic scale. The growth of the particles is therefore only govern by
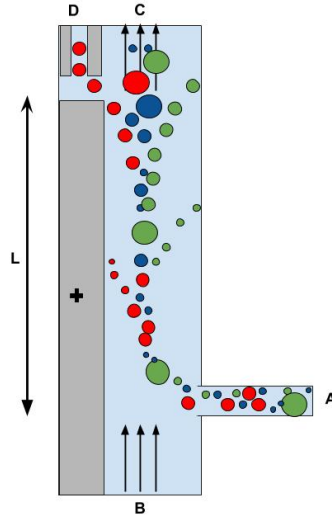
Figure 8: Schematic of the inside of the DMA chamber, (A) is the aerosol inlet, (B) is where the sheath gas flow enter, (C) is where the aerosol and air flow exit and (D) is where the particles with desired charge and size exits. Green particles are positively charged, red are negatively charged and blue are neutral.

particle-particle collisions and does not depend on first forming a larger stable nucleus [12]. This fact makes the composition of the particles material independent and this technique excellent for mixing materials with different vapor pressure and melting point. Different types of material will evaporate and collide at the same rate and the resulting particles will have the same composition as it had in bulk [8]. In the case of stainless steel this is of importance since it is important that all particles contain similar amounts of chromium. The particle composition needs to be as close to the electrodes composition as possible and this is only possible if the collision rate is material independent.

2.3.6 Differential Mobility Analyzer (DMA)

A tandem differential mobility analyzer setup is used in this project. The two DMAs are separated and could function together in series or act solely. The DMA was first proposed by Hewitt (1957) [26] and is a technique to measure the size distribution of charged aerosol particles by relating their mobility in an electric field to their mobility diameter which for spherical particles are identical to their geometric diameter. The DMA is shaped as a cylindrical tube with an inner center rod. Clean sheath gas enters from either the top or the bottom side of the tube and exiting at the opposing side. The aerosol flow is entering from a slit at the same side as the clean sheath flow enters and are mixed together. The center rod is set to either a high positive voltage attracting the negatively charged particles or a high negative voltage attracting the positively charged particles in the aerosol flow. These particles will be pulled toward the inner tube by electrical forces and at the same time pushed upwards by the sheath gas flow. At a distance L from the inlet, an exit slit is located close to the center rod and the particles with preferred electrical mobility will flow into this slit and the rest of the aerosol flow will exit the system with the sheath flow, see Figure 8 [26].

The relation between the central electrical mobility of an aerosol, Z_p, and the parameters inside the DMA was determined by Knutson (1975) [27] and is given by the following equation,

$$Z_p = \frac{q_c + q_m}{4\pi\Lambda V} \tag{7}$$

where q_c and q_m is the clean gas flow rate and the main outlet flow rate respectively, throughout

this project $q_c = q_m$, V is the center rod voltage and Λ is a geometric factor given by

$$\Lambda = \frac{L}{\ln \frac{r_1}{r_2}} \tag{8}$$

where r_1 is the inner radius of the housing, r_2 is the outer radius of the center rod and L is the distance between aerosol inlet and outlet [27]. To use this equation one has to make a few assumptions, for instance, the particles inertia and Brownian motion are neglected and the air flow is assumed to be laminar [27]. The relation between the electrical mobility, Z_p, and the particle mobility diameter, D_p, is given by the following equation,

$$Z_p = \frac{evC_c}{3\pi\mu D_p} \tag{9}$$

where e is the elementary charge, v is the number of charges carried by each particle, C_c is the Cunningham slip correction and μ is the viscosity of air [28]. The Cunningham slip correction describes how small particles are affected by the surrounding gas molecules and increases with smaller particle diameter. The electrical mobility for different sizes and different charged particles for the DMA used in this project are listed in Appendix A.

Based on these equations it is possible to calculate the size of the particles that exits through the slit based on the voltage applied on the center rod. Particles with larger size will have lower electrical mobility and smaller particles will have higher electrical mobility. A simple schematic of the selection of particles is shown in Figure 8. The positively charged particles will be repelled if the center rod was set to a positive voltage and the neutral will not be affected and follow the sheath flow [26]. The smaller negatively charged particles will have a higher electronic mobility and will therefore bend towards the center rod in an early stage. The larger particles with lower electric mobility are not as affected by the center rod voltage and will not bend fast enough and will follow the sheath flow and exit the system [27].

When the size of the particles is measured it assumes that each particle is singly charged. Before entering the first DMA the aerosol flow passes through a bipolar diffusion charger, also known as a neutralizer. Inside the neutralizer, the aerosol flow is exposed to a radioactive source that will charge the particles based on a Boltzmann distribution. Before reaching the neutralizer, the particles have a large variety of charges, due to the high temperature and high ion concentration in the vicinity of the spark, and the charge distribution is completely unpredictable [8]. After the particles have passed through the neutralizer, the charge distribution is highly predictable and based on the size of the particles. Most of the particles will then be neutral but a significant amount will become singly charged and only a few percent will become doubly charged. The amount of singly charged particles depends on the size of the particles and it increases as the size of the particles increases, see Appendix B. For 70 nm aerosol particles 50% will become neutral, 26% negatively singly charged, 19% positively singly charged and <5% doubly or multiply charged after passing through the neutralizer [29]. Since the amount of negatively singly charged particles is higher than the positively singly charged, the center rod in the DMA is set to a positive voltage to obtain as high yield as possible.

Lots of particles are lost as waste each time a DMA is used and only a small fraction passes through the DMA after being charged. This is one of the major drawbacks when size selecting with a DMA. It is difficult to get a narrow size distribution and in the same time a high concentration. Another minor concern is that the particles are measured based on their electrical mobility and this assumes that the particles are perfectly shaped spheres and singly charged. This is not always the case when having a large flow of particles. Particles with different morphology and size could have the same electrical mobility as a spherical particle with the desirable size. Therefore, it will always be a small fraction of rod shaped particles that will exit through the slit even though the geometric shape is not desirable. Also larger particles that are multiply charged will act as a smaller particle and exit through the slit as an artifact. This is normally taken into account when measuring the concentration, however, it is difficult to stop these particles from being deposited onto a wafer and it could be an issue if it is important to have a narrow size distribution [30].

2.3.7 Compaction of agglomerates into spherical particles

Since the particles produced in the chamber are randomly shaped agglomerates consisting of primary particles and the desired end result is spherical nanoparticles with a diameter in the size range of 20-100 nm, they need to be reshaped somewhere. This is done by sintering, or compacting, these agglomerates inside a furnace into spherical particles. The compaction is done in the gas flow and is normally completed in just a few seconds at the right temperature. The compaction behavior of agglomerates into nanoparticles is characterized by a decrease of the mean mobility diameter until reaching the compaction temperature, T_c. After reaching the compaction temperature, the mean diameter of the particles stays constant and the particles starts to reshape internally as the temperature continues to increase [7]. The compaction temperature depends on the material of the particles as well as the initial size of the agglomerates. As a rule of thumb, the ratio between the compaction temperature and the melting temperature of bulk, T_c/T_m, in Kelvin is normally between 1/3 and 1/2 for pure metals and 2/3 for oxides [7, 31]. In the case of stainless steel this compaction temperature should be close to 900°C. This temperature is, however, difficult to predict since it depends on the size of the agglomerates as well as the level of oxidation. A smaller mean mobility diameter before compaction will give a lower compaction temperature [31].

2.3.8 Electrometer

The electrometer is the last part of the setup and is where the nanoparticle concentration is measured. The particles are drawn into the electrometer by an external pump, the charged particles are collected by an electrical-isolated filter and the electrical current drained from the filter is measured. This current is later transformed into a number concentration, N, by using the following equation,

$$N = \frac{I}{en_p q_e} \tag{10}$$

where I is the electrical current, e is the elementary unit of charge, n_p is the number of charges per particle and q_e is the flow rate. Since a doubly charged particle gives twice as much current as a singly charged, the tool will measure one doubly charged particle as two particles instead of one. The actual concentration could therefore be slightly lower than the measured. However, the fraction of multiply charged particles is usually low and sometimes even negligible so although one should be aware of its presence it is not a major concern [32].

2.4 Scanning Electron Microscope (SEM)

A SEM is a commonly used electron microscope to image conducting samples on the sub micron scale. It consists of an electron gun and several electron lenses. The electron gun generates the electrons and accelerates them towards the sample. Before reaching the sample, the electrons are focused into a small spot size, usually <10 nm. The electrons interact with the sample in different ways and are later collected and analyzed. There are several ways to change the output; it is possible to change input values such as, acceleration voltage, emission current, probe size and working distance. When the negatively charged electrons from the beam enters the specimen they interacts with the positively charged protons in the nucleus of the atoms. The beam electron-atom interaction could cause a deflection and give the beam electron a new trajectory. If the beam electron does not loose any kinetic energy at the interaction it is called an elastic scattering. When these electrons later leaves the sample, they are referred to as back scattered electrons (BSE). If the beam electrons instead looses energy and transfer it to another electrons it is called inelastic scattering and the detected electrons are referred to as secondary electrons (SE). Together with SE, X-rays are formed and can be measured. The probability for an elastic scattering to occur increases with atomic number (Z) and decreases with the beam electron energy [33].

The backscatter coefficient, η, increases with Z, making it possible to image Z-contrast. However, this coefficient will saturate at high Z, making this contrast weak for similar and heavy elements. In the case with stainless steel, it is not possible to obtain Z-contrast because iron and

chromium has too similar atomic numbers, 26 and 24. The backscatter coefficient does not vary strongly with acceleration voltage but will depend on what is "inside" the structures, since the penetration depth of the backscattered electrons could be as large as a few μm [33].

The SE electrons are loosely bound outer shell electrons that receive sufficient enough kinetic energy during the scattering to be ejected from the atoms in the specimen. All electrons that leaves the sample with a certain low energy are collected and measured as SE. The secondary electron coefficient, δ, increases with lower beam energy. The probability, p, for a SE to leave the sample is given by the following relation,

$$p \approx \exp(\frac{-z}{\lambda}) \tag{11}$$

where z is the depth and λ is the mean free path due to elastic and inelastic collisions. The maximum depth of emission is said to be around 5λ, where $\lambda \approx 1$ nm for metals. As z increases the probability goes towards zero and this makes SE very useful when imaging the surface of a structure since most of the captured electrons are from the surface-near atoms [33].

2.4.1 Feret Diameter

Since all particles are not perfectly shaped spheres one has to use a mathematical method to calculate the different particle sizes from an image acquired with a SEM. In this report, the Feret diameter is used. It is a way to obtain a 3D estimation of a 2D object and it measures the distance between two parallel tangents facing each other. An average value from multiple orientations is obtained in order to get an accurate value. There are different types of Feret diameters used when estimating the geometric size. The minimum Feret diameter is the smallest distance of all orientations and the maximum Feret diameter is the largest of all orientations [34]. When a particle is close to spherical the minimum Feret measurement might be preferable since a small defect could change the average value substantially. When measuring the size of an agglomerate the minimum Feret diameter is closer to the electrical mobility diameter but the Feret diameter is closer to the actual morphology and geometric size of the agglomerates.

2.5 Transmission Electron Microscope (TEM)

A TEM is also an electron microscope but is a much more powerful tool and can image sub nano scale. It is commonly used to image atom structures in crystals. Unlike the SEM, the TEM also collects the electrons that passes through the sample, thereof the transmission. The electrons that passes through the sample is said to be forward scattered and the amount of forward scattered electrons will increase and the amount of scattering events will decrease as the sample gets thinner. That is desirable since it will generate a stronger and more predictable signal. The characteristics of the scattering events are controlled by incident electron energy and the atomic number of the atom where the beam electrons scatters. The probability for a scattering event to occur is determined by the so called interaction cross section, σ. The forward scattered electrons are collected and forms a diffraction pattern. The elastically scattered electrons are the major source of contrast in TEM images and generates most of the intensity in the diffraction pattern. The positions of the diffracted beams of electrons are determined by the size and the shape of the unit cell of the specimen and the intensities are governed by the distribution numbers and type of atoms in the specimen. There are two types of contrast that are arising during elastic scattering: amplitude contrast and phase contrast. Amplitude is the same as mass-thickness contrast and depends strongly on the atomic number Z and the thickness of the specimen. Mass-thickness is most important contrast if looking at a non-crystal. Phase contrast, arises due to changes in the phases of the scattered electrons and it is very sensitive to small changes in sample thickness and orientation of the specimen and is the reason why it is possible to image atomic structure [35].

2.6   Energy Dispersive X-ray Spectroscopy (XEDS)

In combination with SEM or TEM imaging X-ray energy dispersive spectroscopy (XEDS) is usually performed to obtain the elemental composition of the specimen. With XEDS one can determine what elements that are present as well as to quantify these different elements. The spectrum is obtained when core shell electrons are excited from atoms in the structure. When these electrons are excited, higher level electrons are filling the empty state and emitting X-rays. The energy of these X-rays are element characteristic and is based on what shell level these electrons occupies before filling the empty state, whether it is the K, L or M-level. Each element has its own characteristic spectra and the results obtained can easily be compared with a reference data [35].

The quantitative analyses are performed by measuring the intensity of each peak in the spectra and using the following equation to calculate the fraction between elements,

$$\frac{C_a}{C_b} = k_{ab}\frac{I_a}{I_b} \tag{12}$$

where C is the elemental fractions and $C_a + C_b = 1$, I is the intensity of the peak and k_{ab} is a constant that depends on the materials investigated as well as the acceleration voltage. The value of k_{ab} is determined experimentally and has already been performed for many different material combinations, for instance, k_{CrFe} is equal to 0.9 (±0.006) when the acceleration voltage is 120 kV [35].

3 Experimental Methods

The SDG used in this project is located at the Solid State Physics Department in Fysicum at Lunds University. The DMA used was a *TSI Model 308100* and is noted as DMA1 or the first DMA in the text. The second DMA or DMA2 is an in-house built Vienna-type DMA [36]. The furnace used was a *LTF - tube furnace:151180* and the electrometer was a *TSI Aerosol Electrometer Model 3068B*. Some parameters were kept the same throughout the entire project if nothing else is stated. The carrier gas was nitrogen and the flow rate was kept at 1.68 lpm, the capacitance was 21 nF, the sheath gas flow rate input and output were 10 lpm inside both DMAs, the voltage was set to 10 kV and the pressure inside the system was kept at 1015 mbar. All these values were based on previous experience of the system.

3.1 Housing Chamber Parameters

The electrodes used in this project were stainless steel of type AISI 410 and AISI 430 and were obtained from *Goodfellow*. The elementary content and size of these electrodes are shown in Table 1, in the case with AISI 430 the percentage does not add up, and the last 2 wt.% is an unknown mixture of manganese, carbon, silicon, sulfur and phosphorus. The AISI 410 was rod shaped with a flat surface and had a diameter of 9.5 mm and AISI 430 was also rod shaped with a flat surface and had a diameter of 10 mm. The results did not vary much between the two electrodes regarding response to different parameters, such as spark energy and spark frequency. Therefore a complete study of the two electrodes was not performed and the main focus was on AISI 410.

Table 1: The electrodes used during the project

	Fe (wt.%)	Cr (wt.%)	Diameter (mm)
AISI 410	87.5	12.5	9.5
AISI 430	81	17	10

The initial investigations included measuring the concentration distributions at room temperature for different input variable of stainless steel type AISI 410. The gap distance was altered between 1, 2 and 3 mm and for each gap distance size distribution measurements were obtained with a charging current of 1, 5, 10, 15 and 20 mA. The results obtained became the basis on which the suitable charging current and gap distance were determined. Throughout the rest of the project the charging current of 10 mA and the gap distance of 2 mm were used if nothing else is stated.

3.2 Compaction Study

A compaction study was performed to determine the compaction temperature of the particles to reveal when they became spherical. It was performed by selecting agglomerates with a specific electrical mobility diameter in the first DMA. Then letting these agglomerates compact inside the furnace at different temperatures and lastly measure the new size distribution in the second DMA. The electrodes used were AISI 430 and the two agglomerate sizes selected in DMA1 were 70 nm and 50 nm. The temperature in the furnace varied from room temperature to 1350°C and measurements were taken in steps of 100°C below 600°C and in steps of 50°C at higher temperatures. The scans in the second DMA were performed 30 s after the furnace reached the desired temperature to make sure that the temperature was stable. Each scan included 70 data points with 10 s of measuring between each point.

3.3 Deposition

The particles were deposited onto a small piece of silicon wafer that was located in the middle of the electroplate inside the deposition chamber. Different types of depositions were performed; when monodisperse particles were desired, a scan was first performed in the second DMA to determine the diameter of the peak concentration. When the maximum concentration of polydisperse particles was desired, depositions without any DMA were performed. When depositing the particles, the flow was directed into the deposition chamber and a high positive voltage was applied to the electroplate making all the negatively charged particles stuck to the surface. All particles in the flow will be negatively charged if the aerosol flow has passed through any DMA upon deposition and all particles will then be deposited onto the plate. If the aerosol flow has not passed through any DMA it would contain all type of charges but the electroplate will only attract the negatively charged particles. The positively charged particles will be repelled by the electroplate and the neutral particles does not have enough inertia to be deposited onto the wafer and will exit the deposition chamber together with the carrier gas.

When the aerosol flow only contains of negatively charged particles, the measured concentration in the electrometer will be zero during the deposition since all particles are deposited and the electrometer is located after the deposition chamber, see Figure 4. The deposited concentration were therefore measured before and after each deposition to measure the amount of particles that will be deposited, assuming a stable concentration of particles. The concentrations were many times unstable in a short time range but stable for a longer time period and were estimated based on an average concentration during a 30 s time period. Each sample that was used in this report is described in more detail in Appendix C. Depending on the measured concentration, different deposition times where determined in order to get a good yield for the imaging. The voltage on the electroplate was always set to 6.5 kV.

3.4 SEM imaging

The SEM images were acquired with a *SEM Hitachi SU8010*. The acceleration voltage used was 10 kV and the current was 10 μA and only SE were detected. The samples referred to in the result section are described more in detail in Appendix C.

3.4.1 Particle Concentration Measurements

To measure the particle concentration as well as the size distribution from the SEM images, three images at random locations were acquired with a magnification of 10 000x. The total size of the sample was small enough to assume that the particle concentration stayed constant throughout the entire sample and acquiring random images is therefore a suitable method to obtain the actual size distribution. The images were analyzed using ImageJ [37], the *Threshold* were changed in a routinely way and the images were set into *Smooth* mode to minimize the background noise without changing the appearance of the particles. The tool *Analyze Particles* was used to analyze different parameters such as number of particles, total particle area and Feret diameter. The Feret diameter was later used to determine the geometric diameter of the particles.

3.5 TEM imaging and XEDS spectra

The TEM images were acquired with a 300 kV - *Hitachi 3000F*. Because of the nature of TEM imaging, it is impossible to image from a thick silicon wafer. The particles need to be deposited onto something that electrons can penetrate. Therefore, the TEM samples were prepared by attaching a small carbon coated copper grid onto the silicon wafer using colloidal silver. This copper grid contains of small circular dots and each dot contains of a much smaller grid made of a few carbon layers, see Figure 9. The nanoparticles stuck to the carbon film are imaged by letting electrons penetrate this film. The XEDS spectra was acquired from two nanoparticles and was analyzed using *INCA* software.
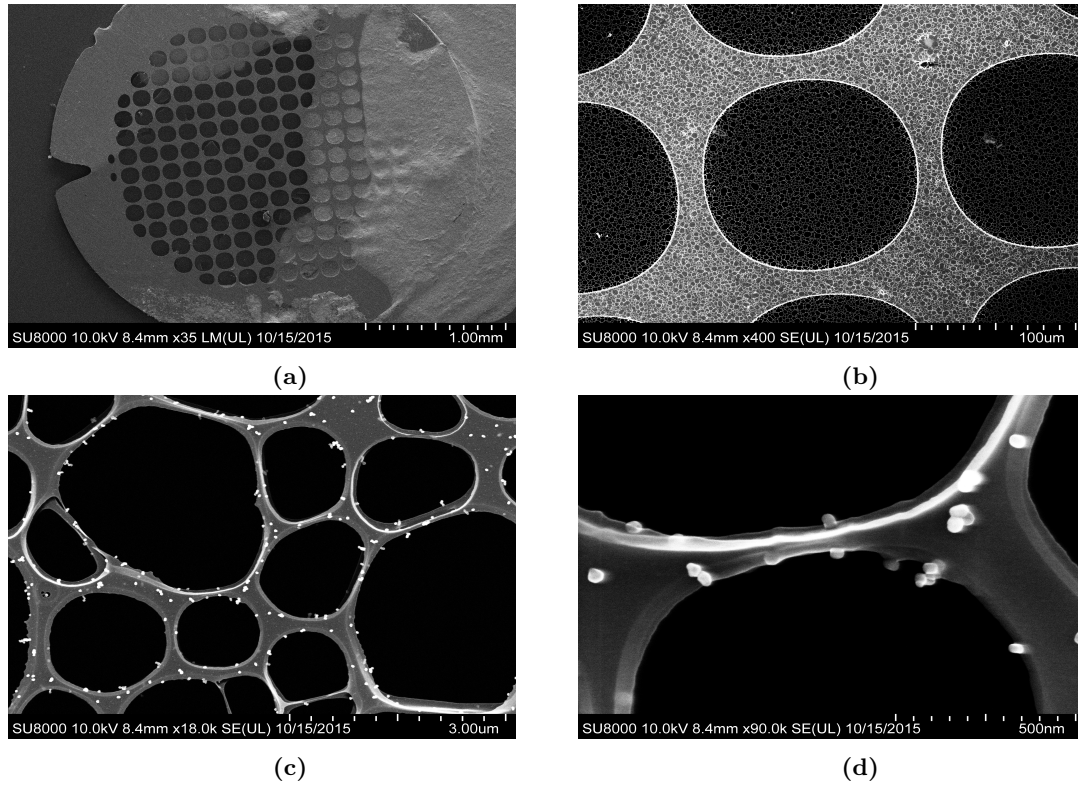
Figure 9: SEM images showing the carbon coated copper grid used when imaging in TEM. The white dots in (c) and (d) are nanoparticles deposited onto the carbon film.

3.6 Deposition using Magnetic Force

To enhancing the sintering behavior of a micro-powder using nanoparticles, the concentration of nanoparticles deposited onto the micro-powder should be as high as possible. The aim was to deposit particles without using any DMA hence having an aerosol flow consisting of neutral, positively charged and negatively charged particles. When using an electroplate to deposit particles, all but the negatively charged particles are lost.

The electrodes used in this project are of type AISI 410 and AISI 430, both of them are soft magnets and are attracted to magnetic forces. It is difficult to know if each particles generated also are soft magnets or if other effects appears on the nanoscale. The magnetic property depends on how many grains that is present in the particle as well as the number of magnetic domains [38] and this has not been investigated before this experiment. But when acquiring SEM images of these particles, it is difficult to maintain focus of the lenses which indicates that particles are magnetic. An experiment was performed to measure whether it is possible to deposit particles due to magnetic forces instead of electrostatic forces. A strong magnet was put inside the deposition chamber and the electroplate was turned off. Particles with an electrical mobility corresponding to 40 and 68 nm were selected in the first DMA and compacted at 1200°C. These particles were then directed to the deposition chamber and the particles that were not deposited onto the magnet exited the deposition chamber and were measured in the electrometer. The concentration was first measured without a magnet for 10 min and then with magnet for 10 min. In total five measurements were obtained to get an average value, started and ended without the magnet in the chamber. The magnet was also put closer to the aerosol gas inlet and finally a lower gas flow, 1 lpm, was used to measure whether the amount of deposited particles changed. The magnet was covered in *Parafilm*® before placed in the chamber to simplify the cleaning of the magnet between depositions.

17

4 Results and Discussion

4.1 Influence of gap distance and charging current

Figure 10 shows the concentration measurements obtained after running the SDG at three different gap distances and at each gap distance, five different charging currents. The concentration of particles increased with larger gap distances due to higher energy of the sparks. The particle size distributions were shifted towards smaller diameters for the 1 mm gap distance but were similar for the two larger distances (2 mm and 3 mm). The peak concentrations were located at approximately 60 nm when the gap distance was 1 mm, 80 nm with 2 mm and finally 90 nm when 3 mm was used as the gap distance. These values were obtained from the mean values of the higher charging currents, larger than 5 mA. When the charging currents were increased, the peak concentrations were at first shifted to the right and the concentration increased but after it reached a maximum at, usually, 10 mA it started to shift towards lower particle sizes and the concentration peaks had a minor decrease. This is best demonstrated when the gap distance was 2 mm, see Figure 10b. All this is in line with earlier reported results and can be explained in theory with an increased breakdown voltage and spark energy when the gap distance is increased and a higher current give rise to a larger spark repetition frequency and therefore a higher concentration [7, 10, 11]. The increase in concentration with respect to frequency should increase somewhat linearly until reaching a point where a higher frequency only leads to a higher degree of coagulation. This will lower the concentration of particles and in order to continue to increase the concentration one has to increase the carrier gas flow rate [11].

The flat top in Figure 10c is due to a limitation in the measurement equipment, the maximum measurable concentration of the electrometer is $2.8 \cdot 10^6$ particles/cm^3, and when this value is reached, a flat line appears instead of a peak. One could also notice more irregularities in Figure 10a compared to the other and this was one of the main reasons for not choosing 1 mm as the gap distance for further studies. Also, since the actual appearance of the distribution in Figure 10c is not exactly known due to the concentration limit, 3 mm was also not used. Based on these results the settings used to obtain further results were 2 mm and 10 mA if nothing else is stated.
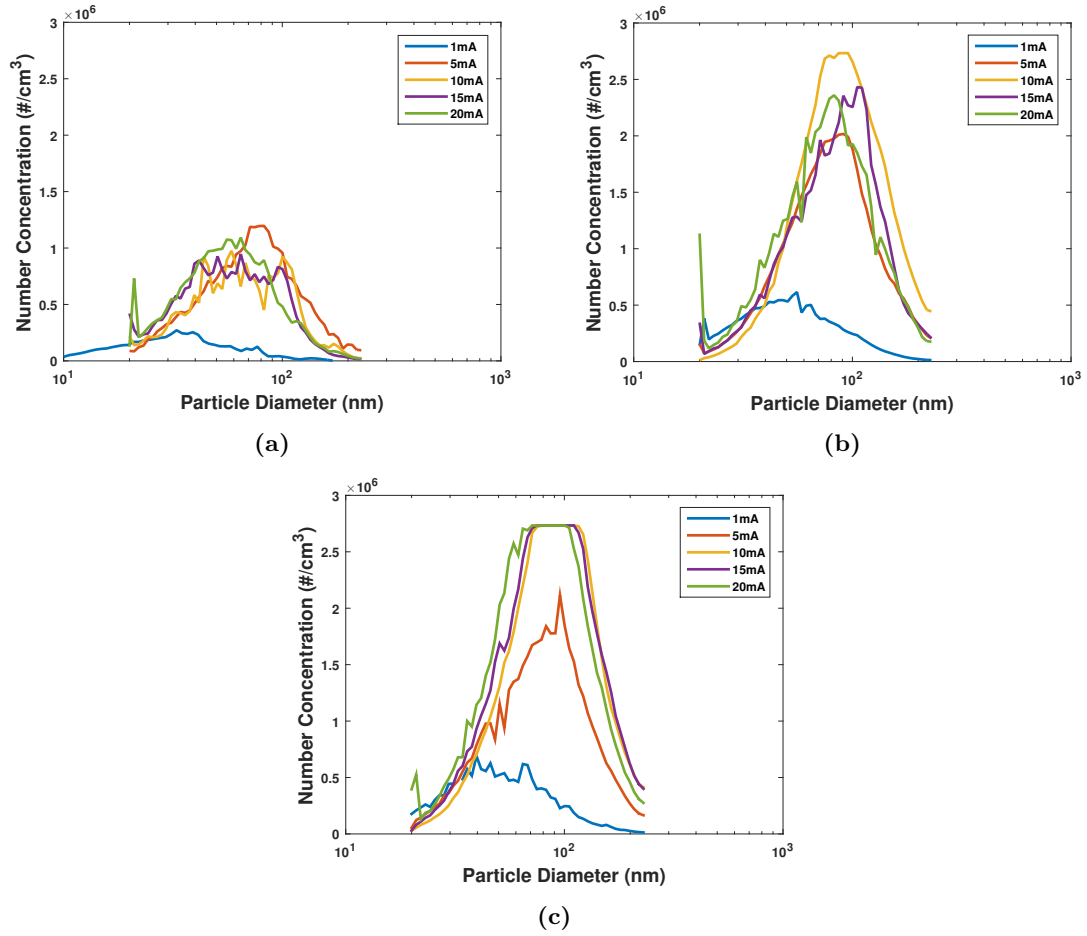
Figure 10: Concentration measurements at (a) 1 mm, (b) 2 mm and (c) 3 mm gap distance with different charging currents.

4.2 Compaction studies

The size distribution and how the electrical mobility diameter changed with increased temperature were measure in order to obtain the compaction temperature for stainless steel nanoparticles. The results are shown in Figure 11. The diameter of the agglomerates shrink slightly until reaching a temperature of about $700-800°$C. At this temperature the shrinking is suddenly significant. In the case with initially 50 nm agglomerates the compaction seem to flatten out at $1200°$C and the new diameter is roughly 35 nm. In the case with the 70 nm agglomerates the decrease continues even at higher temperatures indicating that the compacting was not completely developed at temperatures below $1400°$C. The first DMA selected agglomerates with electrical mobility corresponding to 50 and 70 nm diameter but when reaching the second DMA these diameters are measured as 55 and 75 nm after being compacted at low temperature. The reason for this increase might be due to the fact that different DMAs were used and could have measured the diameter differently. Another reason might be minor coagulation inside the furnace. This appearance has, however, been reported earlier [39].

There are some uncertainties regarding the actual value at some points in Figure 11. The values were determined by performing a DMA2 scan after selecting agglomerates in the first DMA and compacting them at different temperatures, see Figure 4 for a reminder of the setup. When the agglomerates reached the furnace most of the particles were singly charged with a few larger doubly charged particles. But when compacted at higher temperatures there was a risk of thermally charge
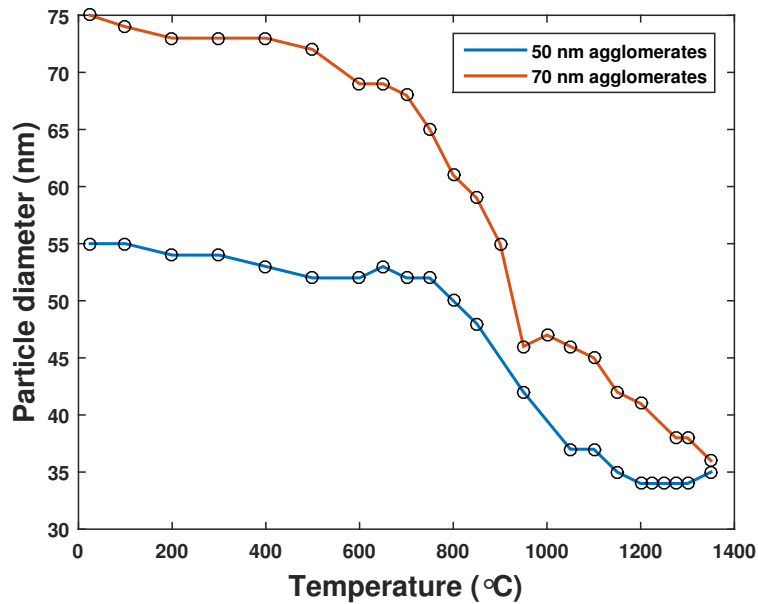
Figure 11: The change of particle electric mobility diameter with increased compacting temperature for 70 nm agglomerates and 50 nm agglomerates. The agglomerates were selected in DMA1 and the new size distributions were obtained in DMA2. At 1200°C, the 50 nm agglomerates had compacted into 35 nm spheres.

these agglomerates/particles from singly to multiply charged particles [39]. These multiple charges will be visible in the DMA scan as peaks located at lower diameters, fooling the computer that smaller particles are present. Figure 12 shows the result after compacting at 800°C. There are three distinct peaks present, each one representing a singly, doubly and triply charged particles. If the rightmost peak is the corresponding to singly charged particles and located at 61 nm then the theoretical double peak should be at 42 nm and the triple peak at 34 nm, see Appendix A. In this case, the theoretical values correspond very well to the experimentally obtained values and the particles are assumed to have an average diameter of 61 nm. SEM images showing these non-compacted particles are displayed in Figure 13.

When the temperature in the furnace was between 800 and 1000°C the particles changed diameter significantly, see Figure 11. In this zone, the peaks obtained from the DMA scan were not as distinct as at lower temperatures. At these temperatures, the peaks corresponding to singly charged particles almost seem to have disappeared and the peaks corresponding to doubly and triply charged particles blend into each other. In the case when the temperature was 950°C, the particles diameter were determined to 46 nm based on where the corresponding doubly and triply charged particles should be located. But this value could easily have been larger or smaller, see Figure 14. The feature with distinct peaks reappears when the temperature is increased further. Figure 15 shows the size distribution after compacting at 1150°C. The peaks that correspond to singly and doubly charged particles are now easy to distinct and SEM images obtained at 1200°C shows that the particles have transformed from agglomerates into compacted particles, see Figure 16.

The difficulties in finding the peaks corresponding to singly charged particles between 900 and 1000°C are due to several reasons. The concentration of singly charged particles decreases and in the same time the amount of multiply charged particles increases. If these peaks are close to each other they could start overlap. Also in this temperature range most of the compaction starts to take place and depending on the shape of the agglomerates, some will compact completely into spheres and some will still be agglomerates, creating less distinct peaks and instead a more even
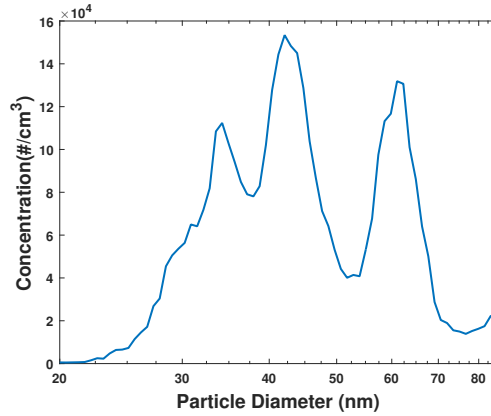
Figure 12: Size distribution of particles obtained by second DMA after compacting at 800°C, three distinct peaks, singly charged at 61 nm, doubly at 42 nm and triply at 34 nm.
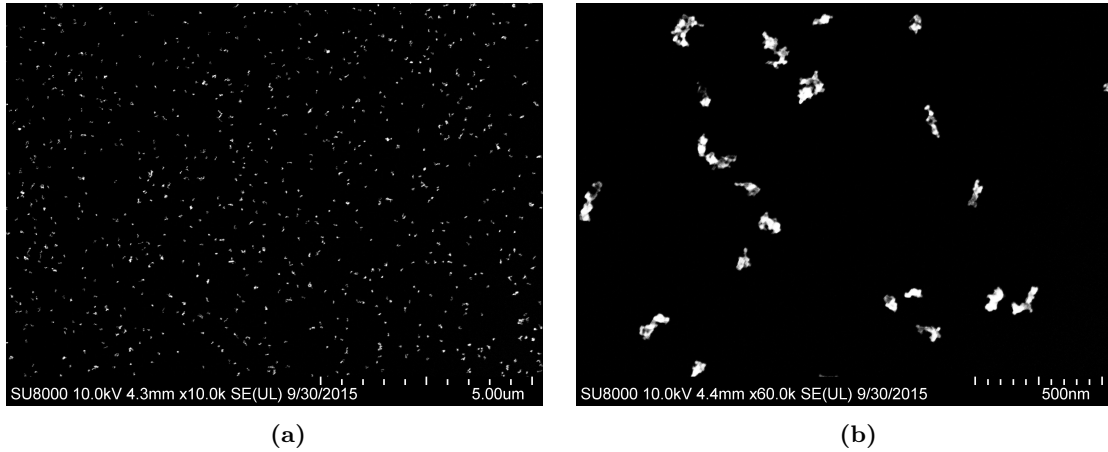

Figure 13: SEM images acquired of Sample 1 after selecting 70 nm agglomerates in the first DMA, compacting at 800°C and selecting doubly and triply charged agglomerates with an electrical mobility corresponding to 38 nm. The left image (a) is an overview and the right one (b) is acquired at a higher magnification. The size distribution is not homogeneous and the agglomerates and has yet not compacted fully.

distribution of sizes. This makes it very difficult and sometimes even impossible to determine an accurate diameter of the particles using only DMA scans.

It has been reported earlier that the compaction temperature decreases when smaller agglomerates are compacted [7, 31]. This effect was difficult to determine in this study, since it was not clear where the compaction temperature was located for 70 nm agglomerates. However, if it would have been possible to increase the temperature above 1400°C, the curve corresponding to 70 nm agglomerates might have flatten out and in that case, the compaction temperature would have been higher for larger agglomerates. One major drawback was the temperature limitations in the furnace. It was difficult to reach temperatures higher than 1350°C which was a necessity to make the particles more spherical and also in order to obtain an accurate compaction temperature for larger agglomerates. The results shown were obtained with AISI 430 as the electrodes, however, the trends when performing similar measurements with AISI 410 electrodes were similar. Therefore, a complete study was not performed and is not included in this report.

This compaction study was performed with nitrogen as the carrier gas and a few measurements were performed with a gas mixture of argon and 5% hydrogen. The results from these measure-
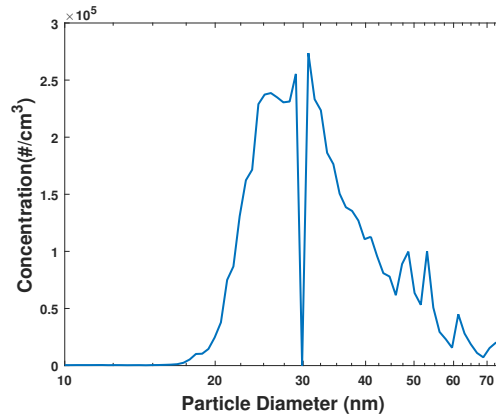
Figure 14: Size distribution of particles after compacting at $950°C$. At this temperature, it is difficult to distinct the different peaks. The doubly and triply charged particles are assumed to be somewhere between 24 and 32 nm. The zero-point at 30 nm is due to measurement error.
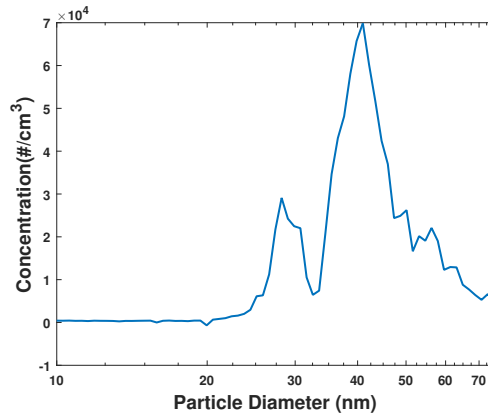

Figure 15: Size distribution of particles after being compacted at $1150°C$. The peak corresponding to singly charged particles is located at 42 nm and the one corresponding to doubly charged particles is located at 29 nm, both are easy to distinguish.

ments were very different from the one with nitrogen at high temperature. The particles seem to be compacted to a much higher degree at lower temperatures compared to when nitrogen was used as the carrier gas. The reason for this might be that the gas mixture with argon and hydrogen prevent oxidation to a greater extent compared to nitrogen. The nitrogen is not pure and could have traces of oxygen present. It has been reported earlier that the compaction temperature for oxidized particles are much higher compared to non-oxidized [31]. Also, the nitrogen could react with the chromium and form nitrides, therefore a different carrier gas is preferable when working with stainless steel. A complete compaction study with argon and hydrogen would have been interesting to perform to investigate whether it is possible to obtain spherical nanoparticles of stainless steel at a temperature much lower than $1200°C$, but was outside the scope of this thesis.
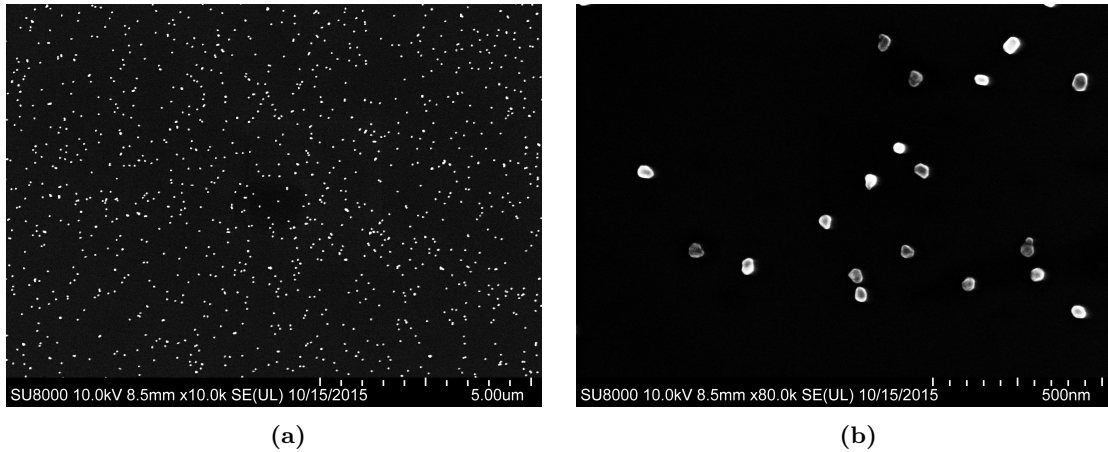
Figure 16: SEM images showing Sample 2. The particles have been compacted at $1200°C$ and then in the second DMA selected with an electric mobility diameter of 28 nm. That is the peak corresponding to doubly charged particles in Figure 15.

4.3 Size Distribution Obtained from SEM Images

The SEM images obtained from Sample 1, that has been compacted at $800°C$, are shown in Figure 13. More details about the parameters used when depositing the different samples are shown in Appendix C. From these images it can be concluded that the agglomerates has not yet fully compacted into spherical particles and are still agglomerates, which is in agreement with the results obtained from the DMA scans of the compacted particles. Figure 17 shows the geometric size distribution of these particles when measuring the Feret diameter. The distribution is wide, includes a large variety of different sizes and the main peak is located at approximately 85 nm. The reason why the peak is located at 85 nm and not 55 nm, as it should be according to the compaction study, see Figure 11, is because of the different ways to determine the particle diameter. The distribution obtained when performing a DMA scan is based on the electrical mobility diameter of the particles and the particles are assumed to be spherical. The distribution obtained from the SEM images, shown as a histogram, is based on Feret measurements, where a geometric analysis of the morphology of the particles has been performed. Particles that are rod shaped might have a very high electrical mobility but in the same time appear as a particles with larger diameter. When most particles are agglomerates there will be a substantial difference between the electrical mobility diameter and the Feret diameter.
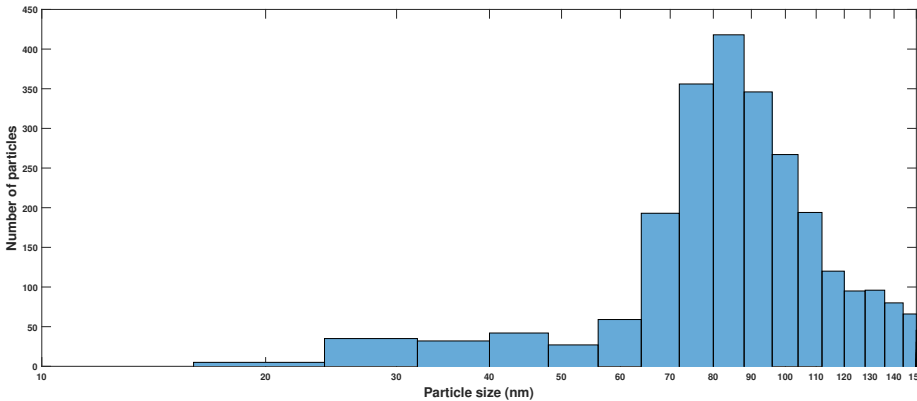

Figure 17: Histogram showing the size distribution of Sample 1 that has been compacted at $800°C$.
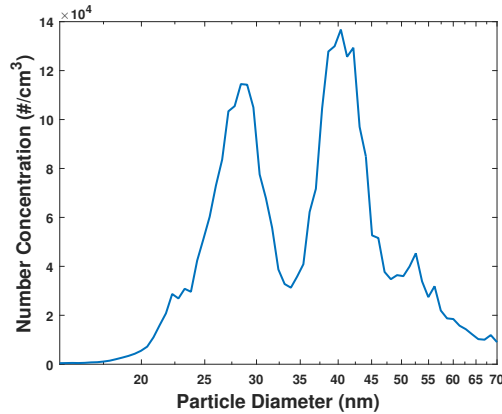
Figure 18: DMA scan after selecting 70 nm agglomerates and compacted at $1200°$C. The two peaks corresponds to singly charged 40 nm particles and doubly charged 40 nm particles appearing as 28 nm particles.

When the temperature was increased to $1200°$C the particles became almost perfectly spherical. Figure 16 shows SEM images of Sample 2 that was compacted at this temperature. Compared to the agglomerates in Figure 13, these particles are much more spherical and the compaction temperature might have been passed. Two different measurements of the geometric size distribution were performed at this temperature in order to conclude that lower peaks in the DMA scan corresponds to doubly charged particles and not smaller particles. The DMA scan at $1200°$C can be seen in Figure 18. Sample 2 and 3 were acquired after first selecting 70 nm agglomerates in the first DMA, compacting them at $1200°$C and then selecting 40 nm particles for Sample 3 and 28 nm particles for Sample 2 in the second DMA before depositing. These values were based on DMA scans performed before deposition, see Figure 18. Figure 19 shows the size distributions of these two depositions. Both histograms has a peak at approximately 60 nm and none of the distributions showed a significant contribution of particles <50 nm, concluding that the second peak corresponds to doubly charged particles and not smaller particles. The reason why the measured geometric size is larger than the electric mobility diameter is, again, because of the different way to estimate the size of the particles. When measuring the Feret diameter, any small defect on the particle will increase the geometric size to a higher degree compared to the electric mobility of the particle.

It is noticeable that the lower distribution, Figure 19b, when selecting the 40 nm peak, has a higher contribution of larger particles. This is because when selecting particles that have an electrical mobility corresponding to singly charged 28 nm particles it will end up with a mixture of singly charged 28 nm, doubly charged 40 nm and a few 50 nm that are triply charged. But when selecting particles with an electrical mobility corresponding to singly charged 40 nm particles the mixture will be, singly charged 40 nm, doubly charged at 58 nm and triply charged at 72 nm. The amount of particles with a charge larger than two is very low even after being thermally charged and by selecting the singly charged peak at 28 nm it will contribute to a lower contribution of larger particles with higher charge and the size distribution becomes narrower.
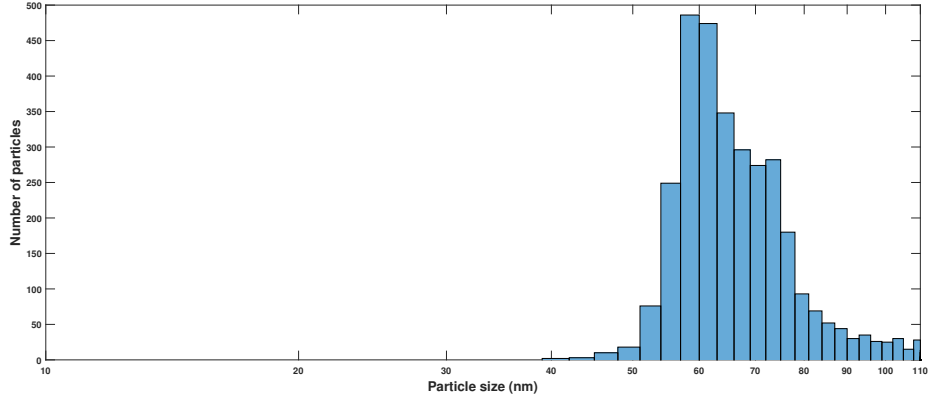
(a)
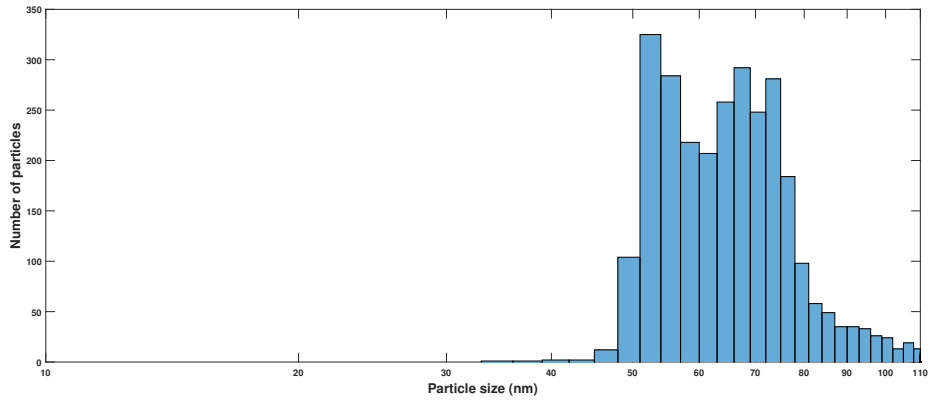
(b)

Figure 19: Histograms showing the size distribution from three randomly acquired SEM images of Sample 2 and 3. Both samples were compacted at 1200°C but different peaks were selected in the second DMA, electric mobility corresponding to (a) 28 nm particles and (b) 40 nm particles.

4.4 Composition of the Nanoparticles

A nanoparticle generated from sample 4 with AISI 430 electrodes and being compacted at 1300°C is shown in Figure 20 and the corresponding XEDS spectrum is shown in Figure 21. The spectra shows peaks at 6.5 keV and 5.4 keV and these peaks corresponds to K_α for iron and chromium respectively. The corresponding K_β peaks are also located next to the K_α peaks. The large peak at 8 keV is due to contribution from the copper grid and the large peaks at <2 keV are due to lighter element contribution such as carbon, nitrogen and oxygen.

This spectrum was also used to perform a rough quantitative analysis of the particle composition based on the intensities of the peaks. By using Equation 12 the average composition of the single nanoparticle in Figure 20 as well as another nanoparticle was estimated to 16.3 wt.% chromium, compared to the electrodes that consisted of 17 wt.% chromium. These results indicate that the particles have a very similar composition as the electrodes and that it exist enough chromium to still maintain the corrosion resistance properties. However, this is the average composition of two nanoparticles and does not conclude whether the rest of the particles have they same or even similar composition although the results are very promising. Unfortunately, no scanning transmission electron microscopy (STEM) was performed. The XEDS data was obtained from the whole particle but with STEM it would have been possible to obtain the composition at different spots on the particle and it would have been interesting to investigate the surface composition of

the nanoparticle. Ideally, chromium oxide should have been formed at the surface to protect the iron from oxidizing but this was not possible to conclude. However, the particles were stable in ambient air long after produced. The particle from Sample 4 in Figure 20 was produced three days before analyzed in TEM.
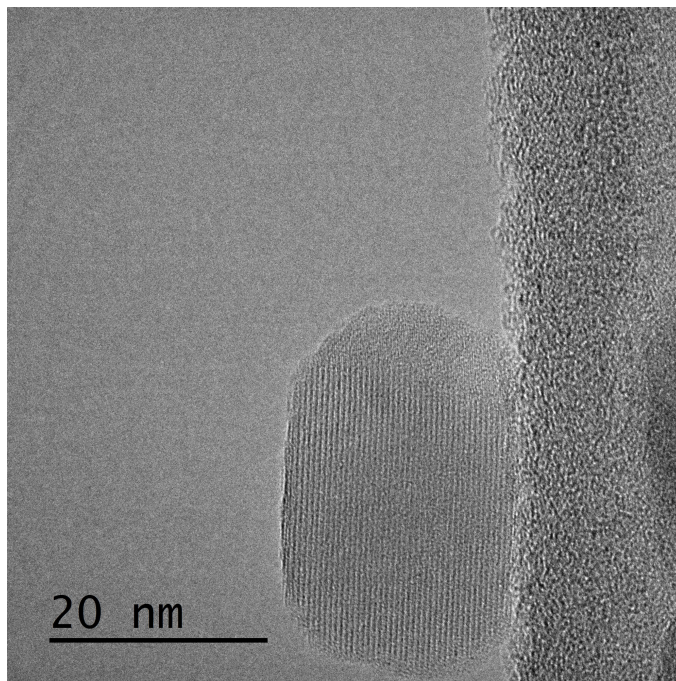

Figure 20: One nanoparticle deposited onto a TEM grid, the features on the right side is the carbon film.
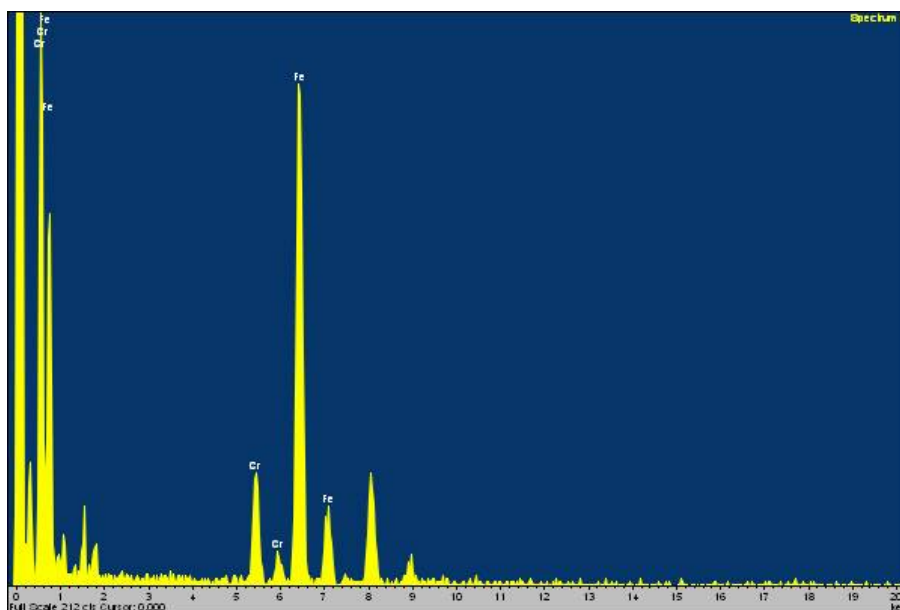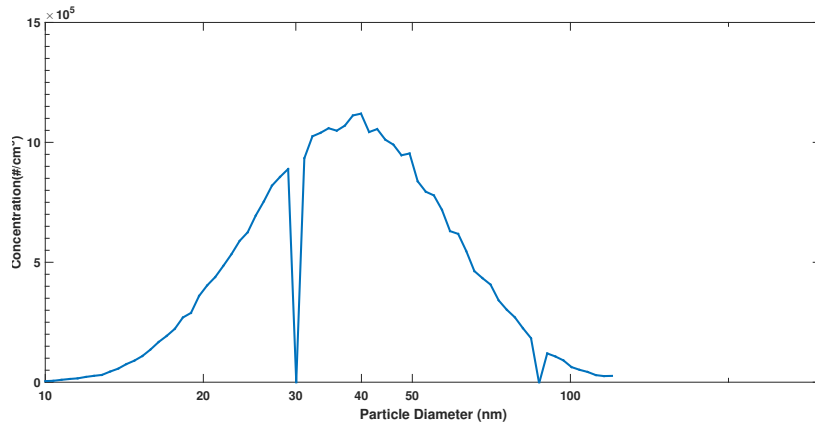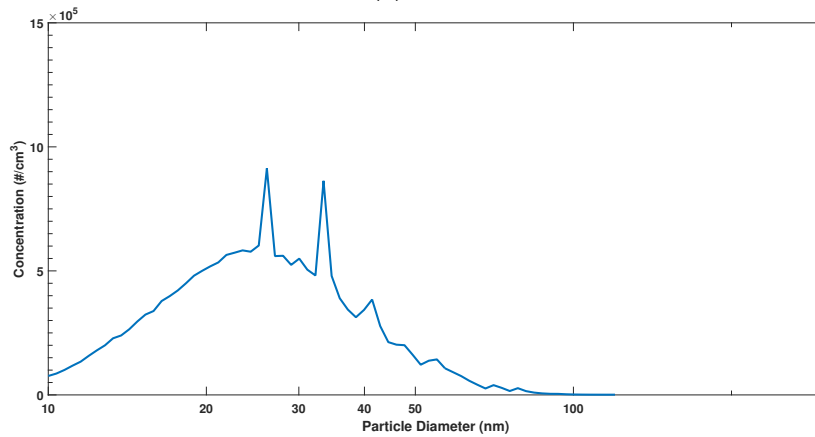

Figure 21: The XEDS spectrum from the particle in shown in Figure 20.

(a) 10mA

(b) 1mA

Figure 22: Size distribution of particles generating with a charging current of (a) 10 mA and (b) 1 mA and compacted at 1200°C. The spikes in (b) as well as the zero value in (a) are due to measurement errors.

4.5 Concentration and Size Distribution After Compaction

In order to obtain a high concentration of polydisperse particles with a morphology that is close to spherical, concentration measurements and depositions were performed without using any DMA. Based on the concentration profile in Figure 10b new concentration curves were obtained with different charging currents, 1mA and 10mA, but at the same distance between the electrodes, 2 mm. This time the particles have passed through the furnace at 1200°C to become compacted, the results are shown in Figure 22. The peak particle concentration was twice as high when the higher charging current was used. The other main difference between the two distributions is that the size distribution is shifted to lower diameters when using a lower charging current and does not include a high amount of particles >100 nm. This could be of interest when the particles are mixed with the micro-powder where the main aim was to get as high concentration as possible of particles in the size range 10-100 nm.

The SEM images in Figure 23 and Figure 24 are acquired from Sample 5 and 6 and shows the morphology of the particles and how these were arranged at the surface. At the lower charging current the particles seem to be evenly spread at the surface but the surface coverage is low. At a higher charging current large cluster containing ~40 nm particles were generated. These clusters did not cover a large amount of the surface but they seemed to be packed in a 3D-structure to an higher extent compared to the features generated with a lower charging current. When depositing
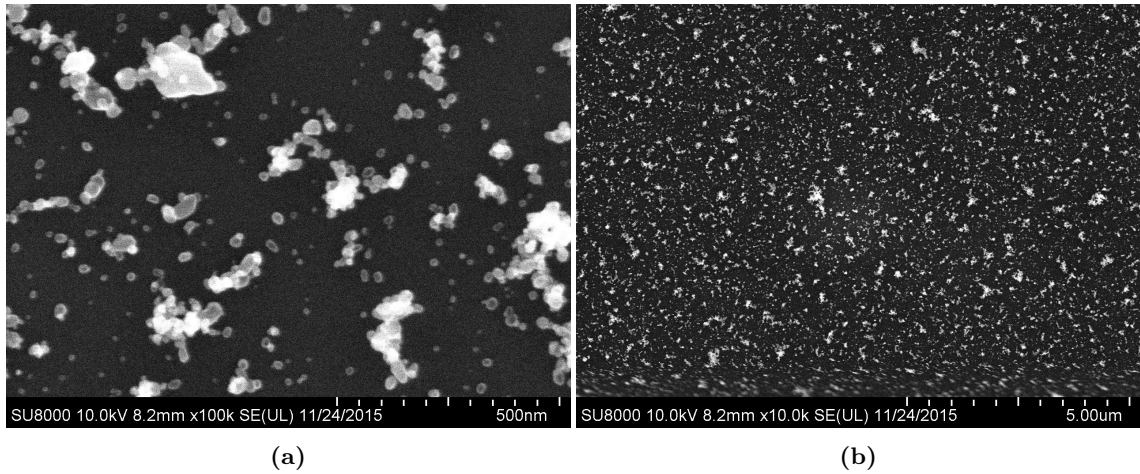
Figure 23: SEM images from Sample 5 with nanoparticles generated with a charging current of 1 mA and compacted at 1200°C.
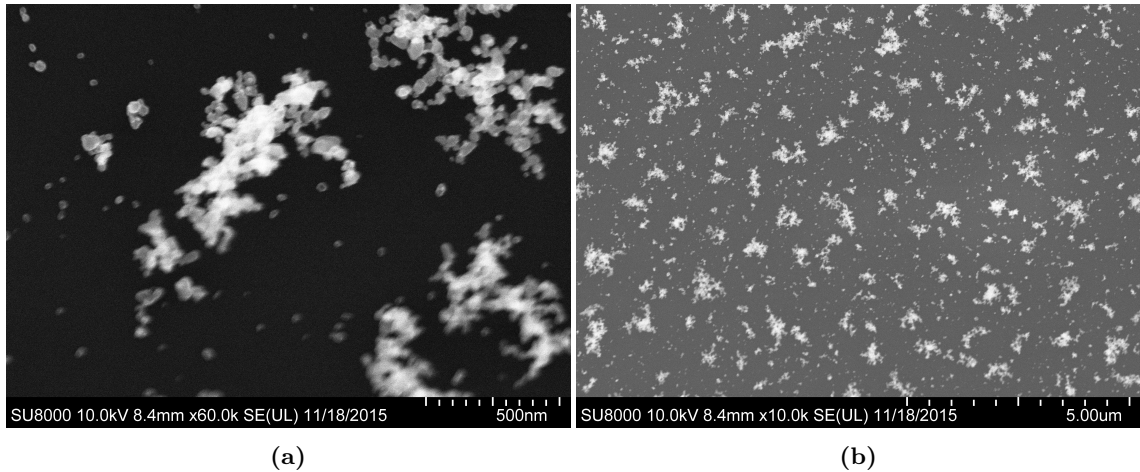

Figure 24: SEM images from Sample 6 with nanoparticles generated with a charging current of 10 mA and compacted at 1200°C.

nanoparticles onto a micro-powder, it is important that as much as possible of the surface of the particles in the micro-powder is covered and, based on these images, that is more likely to happen when using a higher charging current. Based on these result, it is more suitable to use a higher charging current when depositing nanoparticles onto micro-powder.

4.6 Deposition using Magnetic Forces

Since the electrodes used in this project where soft magnets, an experiment was performed to measure whether it is possible to deposit nanoparticles using magnetic force instead of electrostatic forces. Concentration measurements were acquired with and without a magnet present in the deposition chamber. The nanoparticles entered the deposition chamber when the electroplate was turned off and the measured concentrations were the amount of particles that passed the magnet without being deposited, exited the deposition chamber and measured in the electrometer. Ideally the concentration would have reached zero with the magnet present, but this was not the case. Figure 25 shows the result when particle size, distance to magnet and gas flow rate were altered. The main conclusion from these results is that the use of a magnet to deposit nanoparticles onto

a micro-powder is very inefficient and probably not even possible. Even though the presence of a magnet decreased the concentration by a small fraction in all cases, this decrease was not large enough for this technique to be useful. Whether it was because the particles were not magnetic or if it was because the magnetic field was too low is impossible to conclude after performing this type of experiment.

The concentration of particles also depended on the pressure in the system and that was slightly altered between the measurements since the chamber needed to be opened between each measurement to insert and remove the magnet. This is the reason for the slow increase during the first two minutes of measurement. The pressure in the system and in the chamber needs to stabilize before a stable concentration can be obtained.
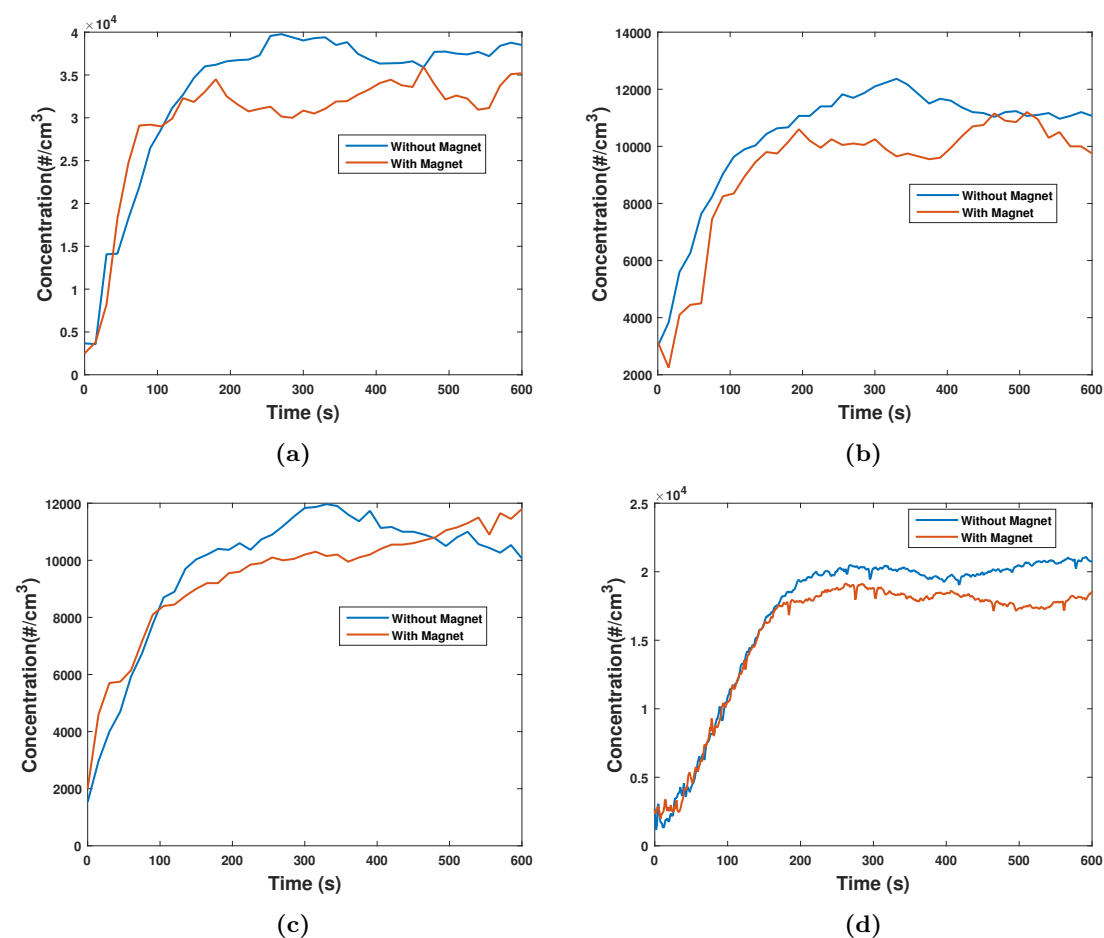

Figure 25: Mean concentration with and without a magnet after depositing for 10 min without any voltage on the electroplate. (a) 40 nm particles, (b) 68 nm particles, (c) 68 nm particles with shorter distance to magnet, and (d) 68 nm particles, short distance and a low flow (1 lpm).

5   Conclusions and Outlook

With this project, it has been shown that it is possible to generate ENP of stainless steel using the SDG. Stable particles with a morphology close to spherical and with a diameter smaller than 60 nm have been produced with almost the same composition as the electrodes used. It has also been shown that when all the agglomerates passes through a furnace and being deposited, a high concentration of nanostructures, consisting of clusters of spherical particles <100 nm, can be obtained with the possibility to enhance sintering of micro-powders. These structures are consumed during sintering and the end product will not consist of any nanostructure, making this a harmless application of nanoparticles. These stainless steel nanoparticles will compact into spherical particles at $\approx 1200°$C when generated using nitrogen as the carrier gas. The results also shows that 10 mA for the charging current and 2 mm as the gap distance are preferable operating parameters to use when the capacitance was 21 nF in order to get a high, stable concentration, that does not vary significantly with time. The main losses of particles when using this technique are occurring when size selecting with a DMA but the use of a DMA could also make the size distributions narrower.

This study of stainless steel nanoparticles generated by a SDG is not completed. More detailed studies regarding the effect of the carrier gas should be performed. So far, only nitrogen has been used and with nitrogen there is a risk of nitride formation or oxidation of the particles and the use of a reducing gas could be a better option. It might also be possible to reach a lower compaction temperature and generate more spherical particles. More studies regarding the properties of the particles also need to be performed, so far only size and morphology have been studied and it would have be interesting to measure the magnetic properties, corrosion resistance and how stable these particles are with time in different environments. More TEM and XEDS analyses need to be performed in order to determine whether the surface of the stainless steel nanoparticles are made of pure chromium oxide or iron oxide, this is of importance since the corrosion resistance depends on this feature. It should also be investigated if all particles produced have the same composition or if this varies significantly between individual nanoparticles. It would be interesting to perform an X-ray diffraction in order to obtain the phases of the particles, if for instance all are ferritic or if it is a mixture of different stainless steel phases.

Investigations with nanoparticles deposited onto a micro-powders needs to be performed. If it is possible to lower the sintering temperature of the micro-powder. When these investigations have been performed and a larger understanding of these stainless steel nanoparticles has been obtained, further experiment regarding applications can be performed. This technique will probably function to produce any types of stainless steel nanoparticles, not only AISI 410 and AISI 430. The applications of these ENP are several, especially if it is possible to increase yield with a factor of 100-1000, it could possibly be used to sinter powders, 3D printing of microstructures and as magnetic tracers.

6   Acknowledgments

7 References

[1] A. Kristensson and B. Martinsson. A beginner's guide to atmospheric aerosol particles, 2015.

[2] L. E. Smart and E. A. Moore. *Solid State Chemistry: an introduction -4 th ed.* Taylor & Francis Group, LLC, 2012.

[3] C. Wang, S. K. Friedlander, and L. Mädler. Nanoparticle aerosol science and technology: an overview. *China Particuology*, 3(5):243–254, 2005.

[4] M. H. Magnusson, B. J. Ohlsson, M. T. Björk, K. A. Dick, M. T. Borgström, and L Samuleson. Semiconductor nanostructures enabled by aerosol technology. *Frontiers of Physics*, 9(3):398–418, 2014.

[5] L. Mädler, H. K. Kammler, R. Mueller, and S. E. Pratsinis. Controlled synthesis of nanostructured particles by flame spray pyrolysis. *Journal of Aerosol Science*, 33(2):369–389, 2002.

[6] N. S. Tabrizi, Q. Xu, N. M. van der Pers, U. Lafont, and A. Schmidt-Ott. Synthesis of mixed metallic nanoparticles by spark discharge. *Journal of Nanoparticle Research*, 11:1209–1218, 2009.

[7] M. E. Messing, K. A. Dick, L. R. Wallenberg, and K. Deppert. Generation of size-selected gold nanoparticles by spark discharge - for growth of epitaxial nanowires. *Gold Bulletin*, 42(1):20–26, 2009.

[8] T. V Pfeiffer, J. Feng, and A. Schmidt-Ott. New developments in spark production of nanoparticles. *Advanced Powder Technology*, 25:56–70, 2014.

[9] N. S. Tabrizi, Q. Xu, N. M. van der Pers, and A. Schmidt-Ott. Generation of mixed metallic nanoparticles from immiscible metals by spark discharge. *Journal of Nanoparticle Research*, 12:247–259, 2010.

[10] B. O. Meuller, M. E. Messing, D. L. J. Engberg, A. M. Jansson, L. I. M. Johansson, S. M. Norlén, N. Tureson, and K. Deppert. Review of spark discharge generators for production of nanoparticle aerosols. *Aerosol Science and Technology*, 46:1256–1270, 2012.

[11] N. S. Tabrizi, M. Ullman, V. A Vons, U. Lafont, and A. Schmidt-Ott. Generation of nanoparticles by spark discharge. *Journal of Nanoparticle Research*, 11:315–332, 2009.

[12] J. Feng, G. Biskos, and A. Schmidt-Ott. Toward industrial scale suthesis of ultrapure singlet nanoparticles with controllable sizes in a continuous gas-phase process. *Scientific Reports*, 5(15788), 2015.

[13] L. Ludvigsson, B. O. Meuller, and M. E. Messing. Investigation of initial particle stages during spark discharge. *Journal of Physics D: Applied Physics*, 48(314012), 2015.

[14] J. D. Verhoeven. *Steel Metallurgy for the Non-Metallurgist.* ASM International, 2007.

[15] M. Ternell. World leaders in steel, 13-05-2015. `http://www.jernkontoret.se/en/the-steel-industry/the-market-for-steel/world-leaders-in-steel/`.

[16] R. M. German. *Powder Metallurgy & Particulate Materials Processing.* Metal Powder Industries Federation, Princeton, NJ, 2005.

[17] J. P. Choi, H. G. Lyu, J. I. Song, W. S. Lee, and J. S. Lee. Sintering behavior of 316l stainless steel micro-nanopowder compact fabricated by powder injection molding. *Powder Technology*, 279:196–202, 2015.

[18] A-K Nyman. Steel industry's important role in society, 20-05-2015. `http://www.jernkontoret.se/en/the-steel-industry/steel-industrys-important-role/`.

[19] D. R Askeland and P. P. Fulay. *Essientials of Materials Science and Engineering.* Cengage Learning, Stamford, CT, 2010.

[20] D. Peckner and I. M. Bernstein. *Handbook of Stainless Steel.* McGraw-Hill, New York, 1977.

[21] J. R. Davis. *Stainless Steels.* ASM International, 2004.

[22] K. Deppert, F. Schmidt, T. Krinke, J. Dixkens, and H. Fissan. Electrostatic precipitator for homogeneous deposition of ultrafine particles to create quantum-dot structure. *Journal of Aerosol Science*, 27:151–152, 1996.

[23] S. Schwyn, E. Garwin, and A. Schmidt-Ott. Aerosol generation by spark discharge. *Journal of Aerosol Science*, 19(5):639–642, 1988.

[24] S. Blomberg, J. Gustafson, N. M. Martin, M. E. Messing, K. Deppert, Z. Liu, R. Chang, V. R. Fernandes, A. Borg, H. Grönbeck, and E. Lundgren. Generation and oxidation of aerosol deposited pdag nanoparticles. *Surface Science*, 616:186–191, 2013.

[25] K. E. J. Lehtinen and M. R. Zachariah. Energy accumulation in nanoparticle collision and coalescence process. *Aerosol Science*, 33:357–368, 2002.

[26] G. W Hewitt. The charging of small particles for electrostatic precipitation. *Transactions of the American Institution of Electrical Engineers*, 76:300–306, 1957.

[27] E. O. Knutson and K. T. Whitby. Aerosol classification by electric mobility: Apparatus, theory and applications. *Journal of Aerosol Science*, 6:443–451, 1975.

[28] K. Ehara, G. W. Mulholland, and R. C. Hagwood. Determination of arbitrary moments of aerosol size distributions from measurements with a differential mobility analyser. *Aerosol Science and Technology*, 32(5):434–452, 2000.

[29] A. Wiedensohler. An approximation of the bipolar charge distribution for particles in the submicron size range. *Journal of Aerosol Science*, 19(3):387–389, 1988.

[30] G. Biskos, V. Vons, C. U. Yurteri, and A. Schmidt-Ott. Generation and sizing of particles for aerosol-based nanotechnology. *KONA Powder and Particle Journal*, (26):13–35, 2008.

[31] M. N. A. Karlsson, K. Deppert, L. S. Karlsson, M. H. Magnusson, M. H. Malm, and N. S. Srinivasan. Compaction of agglomerates of aerosol nanoparticle: A compilation of experimental data. *Journal of Nanoparticle Research*, 7:43–49, 2005.

[32] TSI. *Aerosol Electrometer Model 3068B*, 2015.

[33] J. Goldstein. *Scanning Electron Microscopy and X-Ray Microanalysis.* Kluwer Academic/Plenum, New York, 2003.

[34] H. G. Merkus. *Particle Size Measurments: Fundamentals, Practice, Quality.* Springer Science & Business Media, 2009.

[35] D. B. Williams and C. B. Carter. *Transmission Electron Microscopy.* Springer US, 2009.

[36] W. Winklmayr, G. P. Reischl, A. O. Lindner, and A. Berner. A new electromobility spectrometer for the measurement of aerosol size distributions in the size range 1 to 100 nm. *Journal of Aerosol Science*, 22:289–296, 1991.

[37] W.S. Rasband. Imagej. U.S. National Institutes of Health, 1997-2014.

[38] Y. Liu, D. J. Sellmyer, and D. Shindo. *Handbook of Advanced Magnetic Materials.* Springer Science, 2006.

[39] M. H. Magnusson, K. Deppert, J-O. Malm, J-O. Bovin, and L. Samuelson. Gold nanoparticles: Production, reshaping, and thermal charging. *Journal of Nanoparticle Research*, 1:243–251, 1999.

Appendix A   Particle Electron Mobility

Table 2: The electrical mobility (Z) for singly charged, doubly charged and triply charge particles, with the pressure set to 1015 mbar, the inner and other radius were 5 cm and 6.6 cm respectively and the sheath air flow was 10 l/min

Particle diameter (nm)	Z_{1-} (m$^2 \cdot$ V$^{-1} \cdot$ s^{-1})	Z_{2-} (m$^2 \cdot$ V$^{-1} \cdot$ s^{-1})	Z_{3-} (m$^2 \cdot$ V$^{-1} \cdot$ s^{-1})
5	$8.167 \cdot 10^{-6}$	$1.633 \cdot 10^{-5}$	$2.450 \cdot 10^{-5}$
10	$2.073 \cdot 10^{-6}$	$4.147 \cdot 10^{-6}$	$6.220 \cdot 10^{-6}$
15	$9.357 \cdot 10^{-7}$	$1.817 \cdot 10^{-6}$	$2.807 \cdot 10^{-6}$
20	$5.344 \cdot 10^{-7}$	$1.069 \cdot 10^{-6}$	$1.603 \cdot 10^{-6}$
25	$3.437 \cdot 10^{-7}$	$6.945 \cdot 10^{-7}$	$1.042 \cdot 10^{-6}$
30	$2.449 \cdot 10^{-7}$	$4.897 \cdot 10^{-7}$	$7.346 \cdot 10^{-7}$
35	$1.826 \cdot 10^{-7}$	$3.653 \cdot 10^{-7}$	$5.479 \cdot 10^{-7}$
40	$1.420 \cdot 10^{-7}$	$2.839 \cdot 10^{-7}$	$4.259 \cdot 10^{-7}$
45	$1.139 \cdot 10^{-7}$	$2.277 \cdot 10^{-7}$	$3.416 \cdot 10^{-7}$
50	$9.362 \cdot 10^{-8}$	$1.872 \cdot 10^{-7}$	$2.809 \cdot 10^{-7}$
55	$7.854 \cdot 10^{-8}$	$1.571 \cdot 10^{-7}$	$2.356 \cdot 10^{-7}$
60	$6.698 \cdot 10^{-8}$	$1.340 \cdot 10^{-7}$	$2.009 \cdot 10^{-7}$
65	$5.792 \cdot 10^{-8}$	$1.158 \cdot 10^{-7}$	$1.738 \cdot 10^{-7}$
70	$5.068 \cdot 10^{-8}$	$1.014 \cdot 10^{-7}$	$1.520 \cdot 10^{-7}$
75	$4.479 \cdot 10^{-8}$	$8.959 \cdot 10^{-8}$	$1.344 \cdot 10^{-7}$
80	$3.994 \cdot 10^{-8}$	$7.989 \cdot 10^{-8}$	$1.198 \cdot 10^{-7}$
85	$3.590 \cdot 10^{-8}$	$7.179 \cdot 10^{-6}$	$1.077 \cdot 10^{-7}$
90	$3.248 \cdot 10^{-8}$	$6.496 \cdot 10^{-8}$	$9.744 \cdot 10^{-8}$
95	$2.957 \cdot 10^{-8}$	$5.913 \cdot 10^{-8}$	$8.870 \cdot 10^{-8}$
100	$2.706 \cdot 10^{-8}$	$5.413 \cdot 10^{-8}$	$8.119 \cdot 10^{-8}$

Appendix B   Bipolar Charge Distribution

Table 3: The charge distribution in % at different diameters

Particle Diameter (nm)	-2	-1	0	1	2
1	0	0.47	99.09	0.44	0
5	0	2.21	95.92	1.86	0
10	0	5.03	90.96	4.02	0
20	0.02	11.14	80.29	8.54	0.01
30	0.17	16.35	71.03	12.35	0.10
50	1.13	22.94	58.10	17.20	0.63
70	2.8	26.02	49.99	19.53	1.57
100	5.67	27.42	42.36	20.75	3.24

Appendix C   Deposition

Table 4: The concentration of AISI 410 particles deposit at different temperature and particle size. C_b is the concentration *before* the deposition and C_a is the concentration *after* the deposition. Sample 5 was deposited with 1 mA as the charging current.

Sample	Temperature (°C)	DMA1 (nm)	DMA2 (nm)	C_b (#/cm^3)	C_a (#/cm^3)	Time (min)
1	800	70	38(2+)	140 000	150 000	20
2	1200	70	28	100 000	120 000	20
3	1200	70	40	150 000	110 000	20
5	1200	-	-	N/A	N/A	10
6	1200	-	-	N/A	N/A	5

Table 5: The concentration of AISI 430 particles deposit at different temperature and particle size. C_b is the concentration *before* the deposition and C_a is the concentration *after* the deposition.

Sample	Temperature (°C)	DMA1 (nm)	DMA2 (nm)	C_b (#/cm^3)	C_a (#/cm^3)	Time (min)
4	1300	50	33	40 000	80 000	40